Journal of Iberian Geology
https://doi.org/10.1007/s41513-019-00103-1

RESEARCH PAPER

The granite-hosted Variscan gold deposit from Santo António mine in the Iberian Massif (Penedono, NW Portugal): constraints from mineral chemistry, fluid inclusions, sulfur and noble gases isotopes

Ana M. R. Neiva[1,2] · António Moura[3] · Carlos A. Leal Gomes[4] · Manuel Francisco Pereira[5] · Fernando Corfu[6]

Received: 18 September 2018 / Accepted: 15 March 2019

Abstract
The study area is located in the Central Iberian Zone, a major tectonic unit of the Iberian Massif (Variscan belt). In this region the basement is composed of Cambrian-Ordovician sedimentary and minor volcanic rocks that underwent deformation and metamorphism during the Carboniferous. These metamorphic rocks host ca. 331–308 Ma granitic plutons emplaced during the D_2 extensional and D_3–D_4 contractional deformation phases. The gold-bearing quartz veins from the Santo António mine (Penedono region) occur in granite formed at 310.1 ± 1.1 Ma and post-dated the peak of metamorphism. Gold–silver alloy is included in quartz, but mainly occurs in spaces between grains or micro-fractures within arsenopyrite of all three generations and less in pyrite. Late sulphides and sulphosalts were deposited along fractures mainly in arsenopyrite, and locally surrounding the gold–silver alloy grains. Ferberite, scheelite and stolzite replace arsenopyrite. The abundant aqueous carbonic fluids and the occurrence of a low-salinity fluid and their minimum possible entrapment temperature of 360–380 °C suggest that this gold-forming event began during the waning stages of the Variscan orogeny. The mean $\delta^{34}S$ values of arsenopyrite and pyrite are − 4.7‰ and − 3.8‰, respectively. He–Ar–Ne isotopic data suggest a crustal origin. The ascent of the granite magma has provided the heat for remobilization of gold, other metals and metalloids from the metamorphic rocks. This gold-arsenopyrite deposit has thus similar characteristics as other selected gold-arsenopyrite deposits from the Iberian Massif, but it contains tungstates.

Keywords Gold · Mineralogy · Geochemistry · Fluid inclusions · S, He, Ar, Ne isotopes · Variscan orogeny

Resumen
El área de estudio está ubicada en la Zona Centroibérica, una importante unidad tectónica del Macizo Ibérico (cinturón varisco). En esta región el basamento está compuesto por rocas sedimentarias y volcánicas del Cámbrico-Ordovícico tectonizadas y metamorfizadas durante el Carbonífero. Estas rocas metamórficas sirven como caja de los plutones graníticos datados en torno a 331–308 Ma y que fueron emplazados durante la fase de deformación extensional D_2 y las fases de deformación contraccional D_3 y D_4. Las venas de cuarzo ricas en oro de la mina de Santo António (región de Penedono) que aparecen en un granito datado a los 310.1 ± 1.1 Ma son posteriores al pico metamórfico regional. La aleación de oro y plata se incluye en el cuarzo, pero se produce principalmente en los espacios entre granos o micro-fracturas dentro de arsenopirita de las tres generaciones y menos en pirita. Los sulfuros y sulfuros tardíos se depositaron a lo largo de las fracturas principalmente en arsenopirita, y alrededor de los granos de aleación de oro y plata. Ferberita, scheelita y la estolzita sustituyen a la arsenopirita. Los abundantes líquidos acuosos carbónicos y la presencia de un fluido de baja salinidad y su posible temperatura de atrapamiento mínima en torno de 360-380 ºC sugieren que este evento de formación de oro comenzó durante las etapas finales de la orogenia varisca. Los valores medios de S de arsenopirita y pirita son − 4.7 ‰ y − 3.8 ‰, respectivamente.

Electronic supplementary material The online version of this article (https://doi.org/10.1007/s41513-019-00103-1) contains supplementary material, which is available to authorized users.

Extended author information available on the last page of the article

Published online: 11 April 2019

Los datos isotópicos de He–Ar–Ne sugieren que en el origen de los fluidos mineralizados participa la corteza continental. El ascenso del magma granítico ha provisto el calor para la movilización del oro, otros metales y metaloides desde las rocas metamórficas. Este depósito de oroarsenopirita tiene así características similares a otros yaciamientos con arsenopirita y oro del Macizo Ibérico, pero sin embargo contienen tungstates.

Palabras clave Oro · Mineralogía · Geoquímica · Inclusiones fluidas · Isotopos de S · He · Ar y Ne · Orogenia Varisca

1 Introduction

Gold-only hydrothermal deposits include orogenic gold, intrusion-related gold systems (which may include veins, stockworks, skarns, disseminations, epithermal and replacement types) and Carlin-type gold deposits. In gold-only hydrothermal deposits, gold is very effectively fractionated from other metals (e.g. Garofalo and Ridley 2014). Orogenic gold deposits are shear-hosted deposits developed along strike-slip fault systems linked to late-stage orogenic events (e.g. Groves et al. 2000). Intrusion related gold deposits are developed in magmatic-hydrothermal environments (e.g. Lang and Baker 2001). Variscan gold deposits occur in western-central Europe, e.g. in the Iberian Massif (e.g. Cotelo Neiva and Neiva 1990; Neiva 1994; Vallance et al. 2003; Couto et al. 2007; Neiva et al. 2008; Gómez-Fernández et al. 2012; D'Angelico et al. 2016; Fuertes-Fuente et al. 2016), Massif Central and Bohemian Massif (Martínez Catalán et al. 1997; Goldfarb et al. 2001). The fluid origin of gold deposits has been debated for a long time (e.g. Burrows and Spooner 1989; Lang and Baker 2001); Pitcairn et al. 2006; Lawrence et al. 2013a, b; Rauchenstein-Martinek et al. 2014; Goldfarb and Groves 2015). Some of the postulated mechanisms involve both magmatic and metamorphic, gold-bearing hydrothermal fluids, but others are associated with regional metamorphic fluids, indicating that gold deposits can form from a variety of fluid and metal sources (Lawrence et al. 2013b). Efforts have been directed at understanding the fluid origin of gold deposits particularly from the standpoint of isotopic information including He–Ar isotopic data of fluid inclusions in pyrite (e.g. Kim et al. 2012) and $\delta^{34}S$ of sulphides (e.g. Liu et al. 2016).

The Penedono area, northern Portugal, is located in the Central Iberian Zone (Iberian Massif; Fig. 1a, b) where Carboniferous granitic plutons (ca. 330–307 Ma; Dias et al. 1998; Valle Aguado et al. 2005; Díez Fernández and Pereira 2016, 2017; López-Moro et al. 2017; Pereira et al. 2018) are hosted by Cambrian–Ordovician metamorphic rocks. The tectonic evolution of this zone began in the late Devonian–early Carboniferous (ca. 360–340 Ma; Dallmeyer et al. 1997) with the thrusting of allochthonous units over the Iberian parautochthon and autochthon (Martínez Catalán et al. 2009; Díez Fernández et al. 2013; Díez Fernández and Arenas 2015). The nappe emplacement produced fold-and-thrust shortening in the Central Iberian Zone (D_1). This crustal thickening (D_1 contractional deformation), considered responsible for creating a thermally and gravitationally imbalanced crust (Escuder Viruete et al. 1994; Martínez Catalán et al. 2014; Alcock et al. 2015), was followed by D_2 extension with the development of D_2 extensional shear zones (Díez Balda et al. 1995) and extensive high-temperature and low-pressure metamorphism reaching anatexis (Escuder Viruete et al. 1998; Díez Fernández and Pereira 2016). In the Penedono area, the Pinhel shear zone, with maximum tectonomagmatic activity at ca. 321–317 Ma, represents a shallow-dipping D_2 shear zone formed during the extensional collapse (Díez Fernández and Pereira 2016). Later, the Central Iberian Zone experienced several pulses of subhorizontal shortening with the development of upright folds and strike-slip shearing as identified by the superimposition of D_3, D_4 and D_5 structures (Díez Fernández and Pereira 2016, 2017).

In the Penedono mining camp the deformed granite of the Tabuaço Massif hosts several gold-bearing quartz veins formed during the D_3 contractional event (Sousa and Ramos 1991). Some of these gold veins were already exploited by the Romans and also between 1939 and 1957, producing a total of 100,816 tons (t) of ore with an average grade of about 7.0 g/t Au. Remaining reserves are estimated at about 1200,000 t with an average grade of about 11.5 g/t Au. There are about 105,000 t of ore with about 3.8 g/t Au in the waste dump from past mining (Cathelineau et al. 1993). The Santo António project has an Experimental Mining License and prospecting tests have been undertaken to evaluate the possibility of reopening the mine. Only few papers have been published about the gold mineralization of the Penedono mining camp. Geology, mineralogy, paragenetic sequence and a few chemical analyses of some sulphides, gold and electrum of different gold-bearing quartz veins from the Penedono area are given by Sousa and Ramos (1991). However, different compositions of arsenopyrite and also the minerals gustavite, cannizarite and rooseveltite were not considered. A comparison of the paragenetic sequence of some gold-bearing quartz veins from the Penedono area is presented by Leal Gomes (2000a). A paragenetic sequence and a detailed study of gold–silver alloy grains from gold-bearing quartz veins of Santo António and the relationship to late Variscan deformation effects are given by Leal Gomes (2000 b). But he does not include ferberite, gustavite, cannizarite, covellite, rooseveltite and scorodite. Gold grains from several

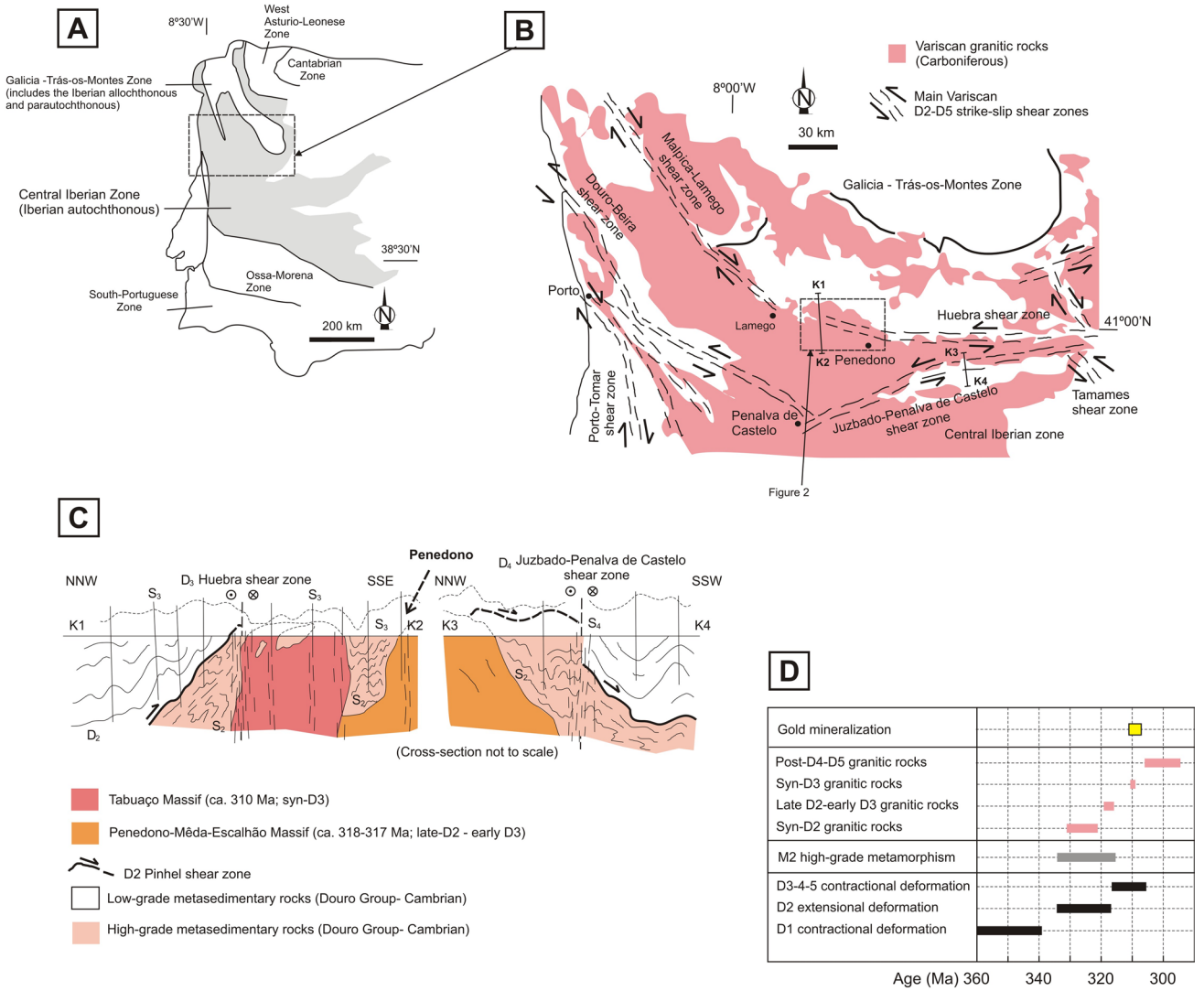

Fig. 1 Geology of the Penedono area, northern Portugal: **a** Location of the study area in the Iberian Massif; **a** shows the location of **b**; **b** schematic representation of the Variscan granitic rocks and main strike-slip shear zones in the Central Iberian zone with location of the Penedono area; **b** shows the location of Fig. 2; **c** cross-sections through the Penedono area (K1–K2) and its southern adjacent area (K3–K4) showing the shallow-dipping D_2 extensional Pinhel shear zone captured and folded by D_3 and D_4 strike-slip shear zones; **b** and **c** adapted from Díez Fernández and Pereira (2016, 2017), Pereira et al. (2018); **d** diagram showing the age variation and time relations of Variscan deformation events, high-grade metamorphism and granitic rocks generation in Central Iberia Zone (adapted from Pereira et al. 2018 and references therein)

Penedono prospects and evidence of mineralization episodes are described by Leal Gomes and Castelo Branco (2003). Fluid inclusion studies of gold quartz veins from the Penedono area were published by Boiron et al. (1996), Nogueira and Noronha (1993) and Noronha et al. (2000).

This paper presents a review of the geology of the Penedono mining camp, with the main focus on paragenetic sequence, chemical compositions of minerals, fluid inclusions studies, S isotopic data of sulphides and He, Ne and Ar isotopic data of fluids from pyrite of Santo António gold-bearing quartz veins to identify the fluid origin of this gold deposit and to discuss the origin. It also reports a new U–Pb age for the granite hosting the deposit. It is a contribution to understand a gold hydrothermal deposit hosted by a S-type granite deformed by Variscan strike-slip systems.

2 Geology

In this section we present a summary of the geological setting of the study area of Penedono located in the Central Iberian Zone and, in particular, of the Santo Antonio shear zone-related gold mineralization developed in granite (Tabuaço Massif).

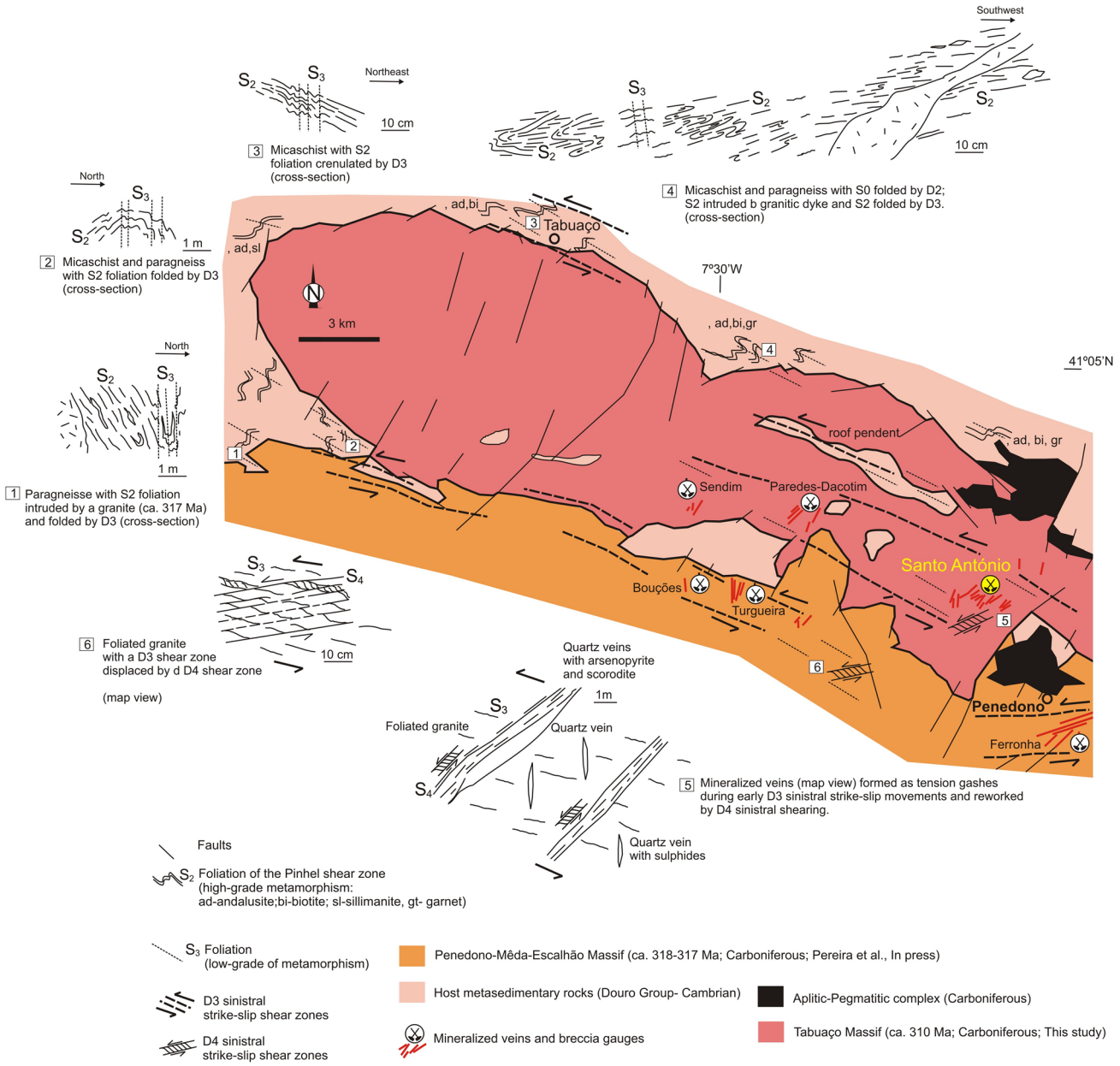

Fig. 2 Simplified geological map of the Penedono area (adapted from Sousa and Ramos 1991; Sousa and Sequeira 1989; Ferreira and Sousa 1994) with reinterpretation of the main Variscan structures

2.1 Geology of the Penedono area

In the study area, the metasedimentary rocks that host the Variscan granitic rocks (Tabuaço and Penedono–Mêda–Escalhão massifs; Figs. 1c and 2) include Cambrian greywackes, siltstones, pelites and limestones (Douro Group) unconformably overlain by Ordovician felsic volcaniclastic rocks (São Gabriel Formation), which are overlain by Ordovician sandstones, siltstones and mudstones (Armorican Quartzite Formation) (Regêncio Macedo 1988; Sousa and Sequeira 1989; Silva and Ribeiro 1991, 1994; Oliveira 1992; Ferreira and Sousa 1994). These Cambrian–Ordovician rocks were transformed into slate, quartzite, phyllite, schist, gneiss and migmatite as a result of variable metamorphic conditions attained during Variscan deformation.

Traditionally, the structure of the Penedono area has been described as the result of two main stages of contractional deformation D_1 and D_3 without recognizing the existence of extensional structures and metamorphism associated with a second deformation stage (D_2). Recently, D_2 structures related to a kilometer-scale extensional shear zone were recognized in the host rocks surrounding the

Penedono–Mêda–Escalhão massif and further south (e.g. Pinhel shear zone; Díez Fernández and Pereira 2016) (Fig. 2). The metamorphic conditions related to the development of this shallow-dipping D_2 shear zone reached partial melting and anatexis (D_2 granites). In the higher-grade metamorphic assemblages S_2 is defined by the growth of sillimanite (fibrolite) and andalusite, garnet and cordierite porphyroblasts and produced an intense overprinting of D_1 structures (Díez Fernández and Pereira 2016). The D_2 extensional Pinhel shear zone was folded during D_3 contraction, and then deformed by D_3, D_4 and D_5 strike-slip shear zones under lower grade metamorphic conditions (Huebra, Lamego-Malpica, Juzbado–Penalva do Castelo and Porto–Tomar shear zones; Díez Fernández and Pereira 2016, 2017) (Fig. 1b).

Accordingly, the Variscan intrusions can be classified in three age groups, including strongly and variably deformed granitic rocks: syn-D_2 (ca. 331–321 Ma), late D_2-early D_3 (ca. 319–315 Ma) and syn-D_3 (ca. 311–310 Ma) (Fig. 1d; Díez Fernández and Pereira 2016; Pereira et al. 2018). The Penedono–Mêda–Escalhão and Tabuaço massifs intruded the D_2 extensional Pinhel shear zone (Figs. 1c and 2). Both plutons were deformed later by the D_3 strike-slip motions along the curved N130–140°E to N80–90°E trending Huebra shear zone (Fig. 1b). This D_3 shear zone was displaced along the N70–80°E trending D_4 Juzbado–Penalva do Castelo shear zone (Fig. 1b).

The Tabuaço Massif is located at the eastern end of the of the N130–140°E trending D_3 Malpica–Lamego shear zone (Llana-Fúnez and Marcos 2001). Mapping suggests that the shear zone merges with the Huebra shear zone (Fig. 1b) and both run parallel to the axial planes of major D_3 folds. The D_3 contractional deformation is responsible for the foliation (S_3) seen in N130–140°E trending sinistral strike-slip shear zones aligned with the strike of the Tabuaço massif. These D_3 strike-slip shear zones control the opening of N50E trending dilatational surfaces that host mineralized quartz veins. The D_4 Juzbado–Penalva do Castelo shear zone drags D_3 folds and continues into the N130–140°E trending Douro–Beira and Tamames shear zones (Díez Fernández and Pereira 2016, 2017). Subsidiary shear zones of this D_4 strike-slip shear zone reworked the preexisting N50E trending mineralized quartz veins (Fig. 2).

The Penedono–Mêda–Escalhão massif (Fig. 2) shows a dominant subvertical magmatic fabric parallel to S_3 and rarely shows a penetrative foliation except for its northern contact locally deformed by the Huebra shear zone. This massif cuts S_2 and occupies the core of a macro-D_3 antiform and so can be considered a late-D_2 to early-D_3 intrusion (ca. 319–318 Ma; Díez Fernández and Pereira 2016; Pereira et al. 2018).

The Penedono mining camp includes several gold prospects, distributed in a 12 km-long and 4 km-wide N100–110°E-trending elongated band within the Tabuaço and Penedono–Mêda–Escalhão granitic massifs (Fig. 2). Important geological features of the camp include: gold-bearing quartz veins hosted by two-mica granites locally hydrothermally altered in the vicinity of vein contacts; vein emplacement controlled by the motion along strike-slip shear zones; in gold bearing mineral assemblages, quartz and arsenopyrite are generally the dominant modal constituents; in peripheral gold-bearing quartz vein walls of 1 m thickness disseminated arsenopyrite and pyrite may also carry gold–silver alloy.

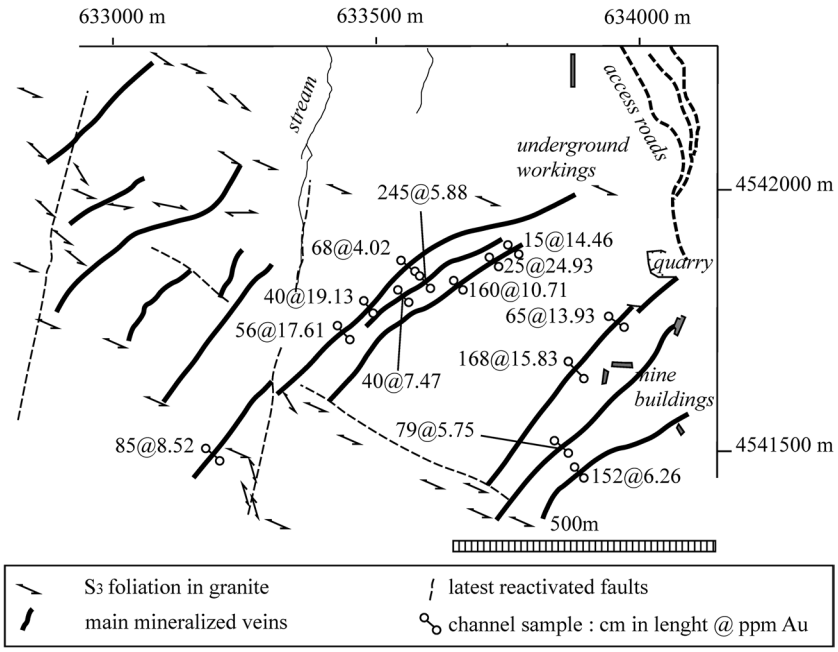

Fig. 3 Geometry of the Santo António quartz vein system and some selected gold contents obtained for channel sampling from early works of Rio Narcea Gold Mines Ltd. (Leal Gomes 2000a)

2.2 Geology and gold setting at the Santo António mine

In the Santo António mine, a system of nearly vertical N40–80°E to N10°E trending quartz veins with less than 3 m width (13 of which have been mined out) intruded a foliated coarse-grained, locally porphyritic, muscovite > biotite granite belonging to the Tabuaço Massif (Fig. 2). Representative gold grades, obtained from analysis of channel samples traversing these veins and related cataclastic gauge structures, as well as some telescoped infillings and hydrothermally altered wallrocks, are located in Fig. 3 and represent the main sector of ancient underground mine works in the Santo António mining camp. The observed results suggest an absence of correlation between the total width of each vein and its gold content and also between the quartz proportion in the veins and adjacent breccia gauges and gold grades. On the contrary there seems to be a more definitive relationship between sulphides presence and gold.

One of the most complex inner vein structures, from a paragenetic and polyphasic deformation point of view, outcrops at the Quarry sector (Fig. 3). It includes most of the major stages of sulphide and gold deposition and thus reflects the progressive and interrelated evolution of deformation and mineralization (Fig. 4).

The inner structural characteristics of the veins may be synthesized by a massive milky quartz that is sheared and recrystallized, and usually does not contain sulphides or gold, but may contain tourmaline. This quartz ± tourmaline assemblage is the main constituent of barren veins. In general, gold-bearing veins show a similar type of quartz ± tourmaline assemblage, forming a barren core surrounded, by vein walls containing sulphides and gold, where arsenopyrite dominates. The arsenopyrite nucleation may eventually propagate into winding fractures affecting inner sub-granulated quartz and corrosion and miarolitic cavities related to hydrothermal alteration or multipulse dilation and deposition in tension voids. Recrystallization and annealed-recovered arsenopyrite correspond to an event that is accompanied by the first expression of free gold (Au–Ag1). Barren veins and gold-bearing veins occur in the same series.

From a broader point of view, shearing reflects a ductile to ductile–brittle behavior and is responsible for a set of fractures that follow the model of Gamond and Giraud (1982). The deduced local deformation and mineralization is polyphasic. As was observed by Leal Gomes and Gaspar (1992) and Leal Gomes (1994, 1997), a coherent model consisting of three main stages of deformation (Sd_1, Sd_2 and Sd_3) and gold mineralization (Au_1, Au_2 and Au_3) accommodated the successive reactivations of the sinistral strike-slip shearing motion following the original opening of earlier tension gashes and formation of major fractures (Figs. 3 and 4). During the more brittle deformation conditions (Sd_2–Sd_3) cataclastic zones with brecciation or the acquisition of crack-seal layered textures were produced in the primary quartz gauges.

The last episodes of brittle deformation (Sd_3) caused reactivation of earlier veins and mineral assemblages and

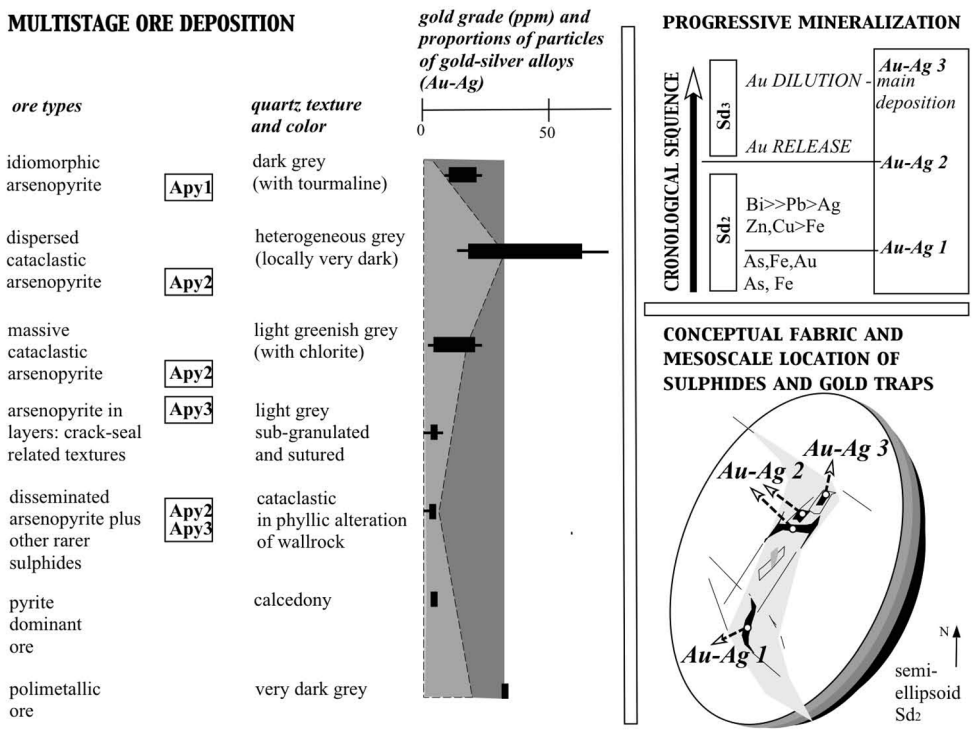

Fig. 4 Diagram of the multistage ore deposition in gold quartz veins, considering the Variscan and post-Variscan deformation (adapted from Leal Gomes 1997, 2000b; Leal Gomes and Castelo Branco 2003). Ars1, Ars2 and Ars3 are the three generations of arsenopyrite presented now

multistage late Pb–Bi–Ag mineralizations, expressed in the crystallization of sulphides, sulphosalts and tellurides, some of which are located in minor transtensive openings (Fig. 4). It also led to remobilization of gold and deposition of electrum, as gold diluted/depleted particles, associated with galena or with chlorite ± carbonates ± fluorite, also recognized in other gold mining sites of NW Portugal (Leal Gomes and Gaspar, 1992).

3 Analytical methods

Our studies include U–Pb monazite and zircon geochronology to obtain the age of the granite from Santo António, and transmitted and reflected light microscopy, electron microprobe analyses, fluid inclusions, microthermometry and Raman spectroscopy, $\delta^{34}S$ data of arsenopyrite and pyrite and isotopic He–Ne–Ar data to characterize the composition of fluids from pyrite of gold-bearing quartz veins.

Monazite and zircon grains for U–Pb dating were separated, using a Frantz magnetic separator and heavy liquids. Afterwards they were handpicked under a binocular microscope and abraded (Davis et al. 1982; Krogh 1982). Uranium and lead isotopic data were measured on a Finnigan MAT 262 multicollector mass spectrometer at the Department of Geosciences, University of Oslo, Norway (Krogh 1973; Corfu 2004). Initial Pb was corrected using Stacey and Kramers (1975) model compositions. The decay constants are from Jaffey et al. (1971). The ISOPLOT 3 Microsoft Excel add-in (Ludwig 2003) was used for the calculation of the U–Pb age.

Channel samples from the Santo António ore deposit were prepared with aqua regia. Gold was determined by induced coupled plasma emission mass spectrometry. The data source is from Rio Narcea Gold Mining Company.

Attempts have been made to date the mineralization through isotopic pyrite analyses by Re–Os at the Department of Earth and Atmospheric Sciences, University of Alberta (Canada), but as the rhenium content is very low (coincident and below the detection limit of 0.03 ppb) it was not possible to date by this method.

The mineral compositions and backscattered images (BSE) were obtained in 55 polished sections using a Hyperbole Jeol JXA-8500 electron microprobe at the National Laboratory of Energy and Geology, S. Mamede de Infesta, Portugal. Sulphides, sulphosalts, gold–silver alloy, native bismuth and arsenates were analysed at an accelaring voltage of 20 kV and a beam current of 20 nA, but tungstates at 15 kV and 10 nA. XPP corrections were applied for sulphides, sulphosalts, gold, electrum, native bismuth, tungstates and arsenates. Standards used include metallic Ni (Ni Kα), metallic Co (Co Kα); synthetic cuprite Cu_2O (Cu Kα); metallic Ag (Ag Lα); metallic Au (Au Mα); sphalerite (Zn Kα); pyrite (Fe Kα, S Kα); $MnTiO_3$ (Mn Kα); CdS (Cd Lα); AsGa (As Lα); galena (Pb Mα); Bi_2Se_3 (Bi Mα); Sb_2S_3 (Sb Lα); metallic pure Nb (Nb Lα); metallic pure Ta (Ta Lα); scheelite (W Lα).

Sulphide grains for the isotope study were hand-picked under binocular microscope. The $\delta^{34}S$ was determined at Actlabs, Canada. Pure pyrite samples and arsenopyrite samples were combusted to SO_2 gas under ~ 10^{-3} torr vacuum. The SO_2 was inlet directly from the vacuum line to the ion source of a VG 602 Isotope Ratio Mass Spectrometer (Ueda 1986). Quantitative combustion to SO_2 was achieved by mixing 5 mg of sample with 100 mg of a V_2O_5 and SiO_2 mixture (1:1). The reaction was carried out at 950 °C for 7 min in quartz glass reaction tube. Pure copper turnings were used as a catalyst to ensure conversion of SO_3 to SO_2. Internal laboratory standards ($SeaWater_{BaSO_4}$ and $Fisher_{BaSO_4}$ were run at the beginning and end of each set of samples (typically 25) and were used to normalize the data as well as correct for any instrument drift. All results are reported in the permil notation relative to the international CDT standard.

Seven pyrite samples were crushed under vacuum for He–Ne–Ar elemental and isotopic compositions. The gas was then purified using hot titanium (750 °C) for 10 min. Noble gases were adsorbed on charcoal at ~ 10 k before being successively desorbed at 32 k, 75 k and 300 k for introduction in the mass spectrometer (Noblesse © from Nu-instruments). Isotopes ^4He and ^{40}Ar were collected on a Faraday cup and measured on a voltmeter using a resistance of 10^{11} ohms. The other isotopes (^3He, ^{20}Ne, ^{21}Ne, ^{22}Ne, ^{36}Ar, ^{38}Ar) were measured using 3 electron multipliers equipped in a pulse counting mode (the noblesse having 3 electron multipliers in order to perform multi-collection). Air standards were analyzed routinely in order to determine the sensitivity and the mass discrimination of the instrument. Blanks were measured before each sample but were negligible compared to the relatively high noble gas abundances of the samples. The results presented are the concentrations expressed in ccSTP/g (cm^3 of gas at standard T and P). The isotopic ratios are corrected for blank and mass discrimination. The data were obtained in the Institut de Physique du Globe de Paris by the Equipe Geochimie & Cosmochimie.

Petrography, microthermometry and Raman analyses of fluid inclusions have been carried out at DGAOT laboratories (Science Faculty, Porto University), in doubly-polished wafers of about 150–200 µm thickness. Microthermometric characterization of the fluids was performed using a Chaixmeca heating-freezing stage (Poty et al. 1976) for cooling experiments, and a Linkam THMSG 600 stage (Shepherd 1981) for the heating experiments. Calibration was carried out with natural and synthetic fluid inclusion standards at $T \leq 0$ °C and with melting-point standards at $T > 25$ °C. The accuracy was ± 0.1 °C during cryometric

measurements and ± 1 °C during heating. Volumetric proportions between volatile and aqueous phases were estimated optically at room temperature by reference to Roedder (1984) and Shepherd et al. (1985) charts. Molar fractions of CO_2, CH_4 and N_2 were determined by Raman microspectroscopy analyses in selected individual inclusions using a Labram Dilor–Jobin–Yvon Spectrometer attached to an Olympus microscope. The excitation source was a He–Ne laser with 632.8 nm wavelength operated at 20 mW. Measurement of the N_2 signal from the air was done immediately after each fluid inclusion analysis. The quantification of the different gas species in the inclusions was obtained using a computer program that follows routine procedures described by Prieto et al. (2012). Salinity (expressed as equivalent wt% of NaCl) of the aqueous inclusions was calculated from microthermometric data using the revised equation of Bodnar (1993). Bulk compositions of both types of fluids were calculated using Bakker (2003) codes. Isochores for the aqueous carbonic fluids were calculated using Bakker (2003) software based on Bakker (1999) and Bowers and Helgeson (1983) equations of state. The isochors for the H_2O–NaCl inclusions were calculated from the equation of state of Knight and Bodnar (1989).

Table 1 Mineral paragenesis of gold-bearing quartz veins from the Santo António mine, Penedono, northern Portugal

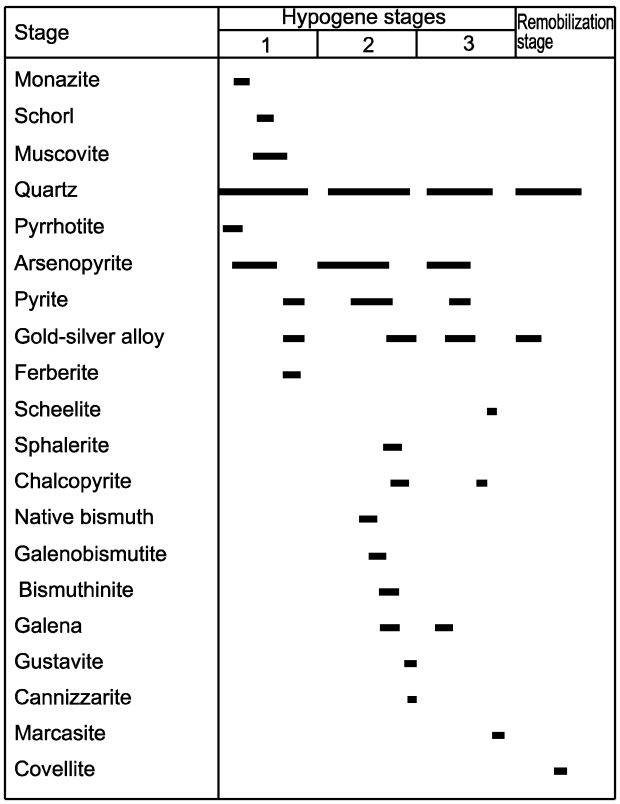

4 Paragenetic sequence of Santo António gold quartz veins

The paragenetic sequence (Table 1) was determined with microscopic mineralogy and electron microprobe analyses by us (Tables 2 and 3; Online Appendices A and B) in combination with earlier publications (Sousa and Ramos 1991; Leal Gomes and Castelo Branco 2003) and two unpublished reports (Cathelineau et al. 1993; Leal Gomes 2000b). Three main stages (1, 2 and 3) of ore deposition and a late hydrothermal remobilization stage are distinguished (Table 1). Chemical analyses of sulphides, sulphosalts and native bismuth from Santo António gold-bearing quartz veins are given in Table 2. Those of gold–silver alloy are presented in Table 3. Chemical analyses of tungstate minerals and arsenates are given in Online Appendices A, B, respectively. The gold–silver alloy grains range from < 10 to 30 × 20 µm and rarely are > 100 µm.

4.1 Stage 1

Schorl is rare, subhedral, brown in colour and intergrown with muscovite. The muscovite is frequent, fine-grained, subhedral and radial and has rare monazite inclusions. Quartz (Qz1) dominates, is anhedral, dark grey with undulatory extinction and deformation bands. Pyrrhotite ($Fe_{0.90}S_{1.01}$) is monocline, rare, euhedral, but mainly anhedral. Arsenopyrite (Apy1) (Fig. 5a) is As-rich and S-deficient (Fig. 6a, b) frequent, euhedral, subhedral and fractured. It has monazite and pyrrhotite inclusions. Pyrite (Py1) (Fig. 6a, c) is rare, anhedral and has pyrrhotite inclusions. Anhedral gold–silver alloy (Au–Ag1) grains occur associated with micro-fractures and between grains of arsenopyrite (Apy1) (Fig. 5a). Rare ferberite is anhedral, occurs as inclusions in quartz (Qz1) and partially replaces arsenopyrite (Apy1) and quartz (Qz1) (Fig. 5b). It contains 8.4 mol% MnO4 (Online Appendix A).

4.2 Stage 2

Quartz (Qz2) is grey, clearer than quartz (Qz1), microgranular and rarely deformed. It contains rare inclusions of monazite. It penetrates along micro-fractures of quartz (Qz1) and surrounds stage 1 sulphides. Arsenopyrite (Apy2) is As-deficient and S-rich, abundant, anhedral, surrounds ferberite and is fractured. Pyrite (Py2) is frequent and anhedral. Gold–silver alloy (Au–Ag2) grains are anhedral and occur filling micro-fractures and in spaces between grains of arsenopyrite (Apy2) (Fig. 5c), but are rarely zoned and included in quartz (Qz2) (Fig. 5d). Sphalerite is rare, anhedral and occurs filling micro-fractures of arsenopyrite (Apy2) and contains up to 2.59 wt% Fe. Rare chalcopyrite is anhedral

Table 2 Selected electron-microprobe chemical analyses in wt% of sulphides, sulphosalts and native bismuth of gold-bearing quartz veins from the Santo António mine, Penedono, northern Portugal

	Ni	Co	Cu	Ag	Zn	Fe	Mn	Cd	As	Pb	Bi	S	Total
Pyrrhotite	–	–	–	–	–	60.85	–	–	–	–	0.09	38.98	99.92
Arsenopyrite (1st generation Apy1)													
With pyrrhotite inclusions	0.02	0.05	–	–	–	33.27	–	–	47.07	–	0.02	19.62	100.05
With gold–silver alloy Au–Ag1	–	0.05	–	–	–	33.81	–	–	47.25	–	0.05	19.14	100.30
Replaced by ferberite	0.03	0.06	–	0.01	–	34.00	–	–	46.16	–	0.06	19.21	99.53
Arsenopyrite (2nd generation Apy2)													
Surrounding ferberite	–	0.06	–	0.02	–	34.08	–	–	45.45	–	0.03	20.60	100.24
With gold–silver alloy Au–Ag2	–	0.02	–	–	–	34.00	–	–	45.93	–	0.04	20.24	100.23
With sulphides and sulphosalts	–	0.06	–	–	–	33.75	–	–	46.08	–	0.06	20.05	100.00
Arsenopyrite (3rd generation Apy3)	–	–	0.01	0.01	0.04	35.28	–	–	42.36	–	0.13	22.14	99.97
Zoned arsenopyrite													
Darker core (2nd generation Apy2)	–	–	–	–	–	34.08	–	–	45.65	–	–	20.60	100.33
Lighter rim (3rd generation Apy3)	–	–	0.01	–	–	34.68	–	–	43.28	–	0.09	22.32	100.38
Pyrite (1st generation)	–	–	–	–	–	46.57	–	–	–	–	0.14	53.06	99.77
Pyrite (2nd generation)	–	–	–	–	–	46.19	–	–	0.01	–	0.16	53.47	99.83
Pyrite (3rd generation)	–	–	–	0.02	–	46.46	–	–	0.01	–	0.17	53.28	99.94
Sphalerite	–	–	–	–	63.46	2.59	0.02	0.54	–	–	–	33.30	99.91
Chalcopyrite	–	–	33.96	–	–	30.25	–	–	–	–	0.13	35.50	99.84
Native bismuth	–	–	–	–	–	0.36	–	–	–	–	99.74	–	100.10
Galenobismutite	–	–	–	–	–	–	–	–	–	29.50	53.30	16.75	99.55
Bismuthinite	–	–	–	–	–	–	–	–	–	–	80.86	19.13	99.99
Galena	–	–	–	2.11	–	–	–	–	–	79.29	4.93	13.73	100.06
Gustavite	–	–	–	8.73	–	–	–	–	–	21.47	53.01	16.44	99.65
Cannizzarite	–	–	–	–	–	–	–	–	–	36.57	47.00	16.42	99.99
Marcasite	–	–	–	–	–	46.50	–	–	–	–	–	53.25	99.75
Covellite	–	–	64.68	–	–	–	–	–	–	–	–	35.10	99.78

Gold–silver alloy associated with micro-fractures and filling spaces between grains of arsenopyrite; Au and Sb were not detected in sulphides and sulphosalts

– not detected

Table 3 Representative electron-microprobe analyses in wt% of gold–silver alloy grains of gold-bearing quartz veins from Santo António, Penedono, northern Portugal

	Associated with fractures in arsenopyrite							Included in quartz 2		Remobilized
	Gold–silver alloy 1		Gold–silver alloy 2			Gold–silver alloy 3		Gold–silver alloy 2		Gold–silver alloy 4
Au	83.39	72.96	83.54	94.50	64.70	80.96	64.46	80.05	52.86	94.78
Ag	16.08	26.45	15.55	4.89	34.57	18.84	34.80	18.81	47.14	4.65
Bi	0.53	0.56	0.63	0.63	0.59	0.30	0.52	0.64	0.35	0.59
Total	100.00	99.97	99.72	100.02	99.86	100.10	99.78	99.50	100.35	100.02
Fineness	838	734	843	951	652	811	649	810	529	953

Gold–silver alloy 1 is within fractures and between grains of arsenopyrite Apy1. Gold–silver alloy 2 and gold–silver alloy 3 are within fractures and between grains of arsenopyrites Apy2 and Apy3, respectively. Fineness [1000 wt% Au/(wt% Au + wt% Ag)] (Fischer 1945)

and partially surrounds pyrite (Py2) and sphalerite. Native bismuth contains up to 0.36 wt% Fe, is rare, anhedral, associated with micro-fractures in arsenopyrite, partially surrounds gold–silver alloy (Au–Ag2) and occurs included in quartz (Qz2) (Fig. 5d). Galenobismutite ($Pb_{1.09}Bi_{1.95}S_4$) is anhedral, rare and occurs associated with micro-fractures of arsenopyrite, where is partially surrounded by quartz (Qz2) (Fig. 5e). Bismuthinite ($Bi_{1.94}S_3$) is rare, anhedral, partially

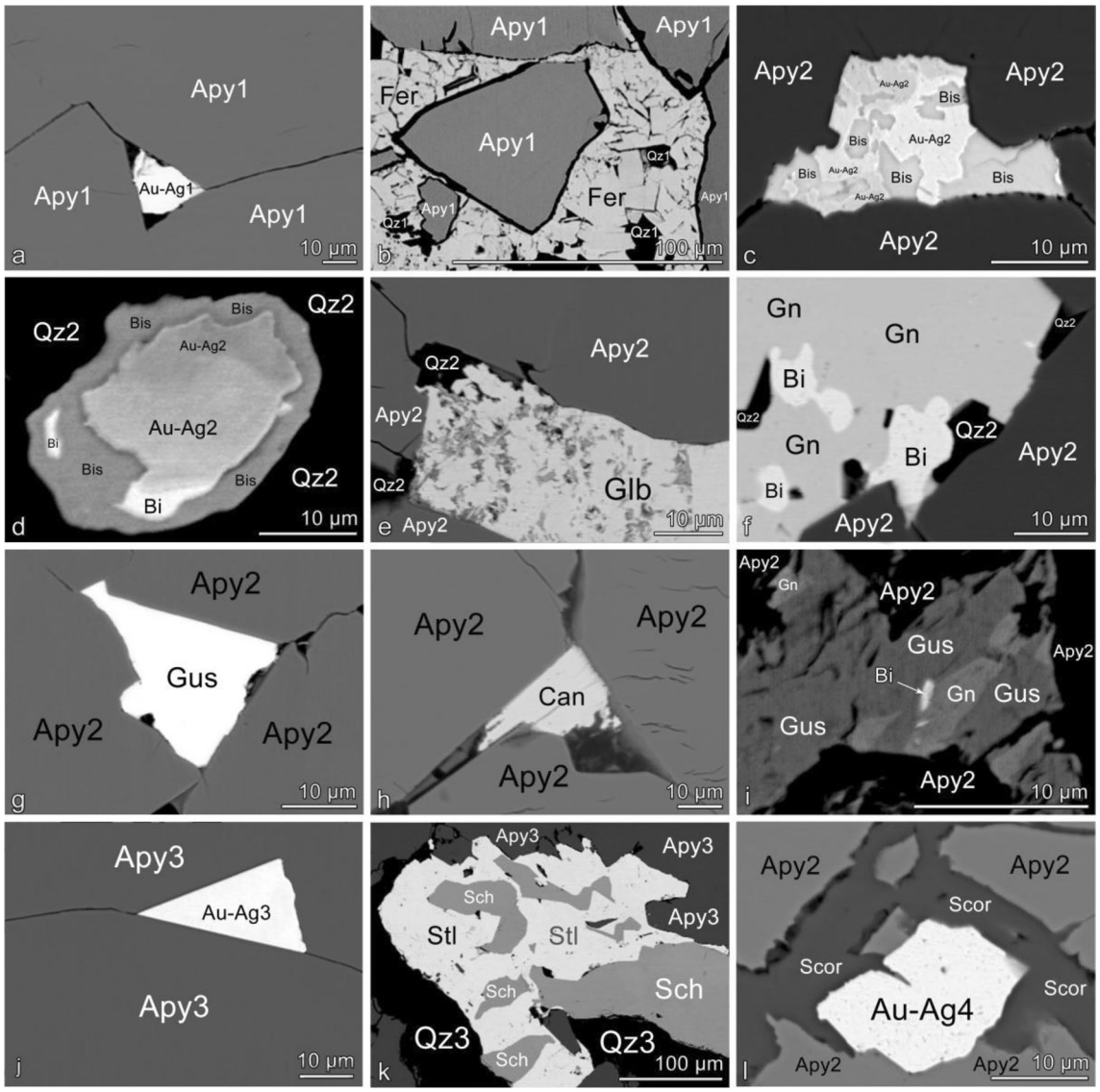

Fig. 5 Backscattered electron images of ore minerals from gold-bearing quartz veins of the Santo António mine. **a** Gold–silver alloy (Au–Ag1) grain penetrated a space between grains of arsenopyrite Apy1 grains. **b** Ferberite (Fer) associated with micro-fractures of arsenopyrite (Apy1) partially replaced this sulphide and quartz (Qz1). **c** Gold–silver alloy (Au–Ag2) grains partially penetrated and surrounded by bismuthinite (Bis) are associated with micro-fractures of arsenopyrite (Apy2). **d** Gold–silver alloy (Au-Ag2) grains mainly surrounded by bismuthinite, which has native bismuth (Bi) inclusions and all are included in quartz (Qz2). **e** Galenobismutite (Glb) partially surrounded by quartz are both associated with micro-fractures of arsenopyrite (Apy2). **f** Galena (Gn) containing inclusions of native bismuth and quartz (Qz2) is in contact with arsenopyrite (Apy2). **g** Gustavite (Gus) filling a space between crystals of arsenopyrite (Apy2). **h** Cannizzarite (Can) fillings a space between crystals of arsenopyrite (Apy2). **i** Galena containing a small inclusion of native bismuth is surrounded by gustavite and they replace arsenopyrite (Apy2). **j** Gold–silver alloy (Au–Ag3) grain penetrated along intercrystalline boundaries of arsenopyrite (Apy3). **k** Stolzite (Stl) with inclusions of scheelite (Schl) associated with quartz (Qz3) and arsenopyrite (Apy3). **l** Gold–silver alloy (Au–Ag4) grain associated with micro-fractures in arsenopyrite (Apy2) and mainly surrounded by scorodite (Scor)

penetrated and surrounded gold–silver alloy (Au–Ag2) grains, some associated with micro-fractures and filling spaces between arsenopyrite grains and others included in quartz (Qz2) (Fig. 5c, d) but of similar composition. It has native bismuth inclusions (Fig. 5d). Galena is anhedral, not frequent, has inclusions of quartz (Qz2), native bismuth (Fig. 5f) and bismuthinite. It occurs included in arsenopyrite (Apy2) and associated with micro-fractures of arsenopyrite (Apy2). Gustavite ($Ag_{0.95}Pb_{1.21}Bi_{2.97}S_6$) and cannizzarite ($Pb_{7.93}Bi_{10.10}S_{23}$) are anhedral, very rare and occur filling spaces between arsenopyrite (Apy2) grains (Fig. 5g, h). Gustavite also partially surrounds galena (Gn) (Fig. 5i).

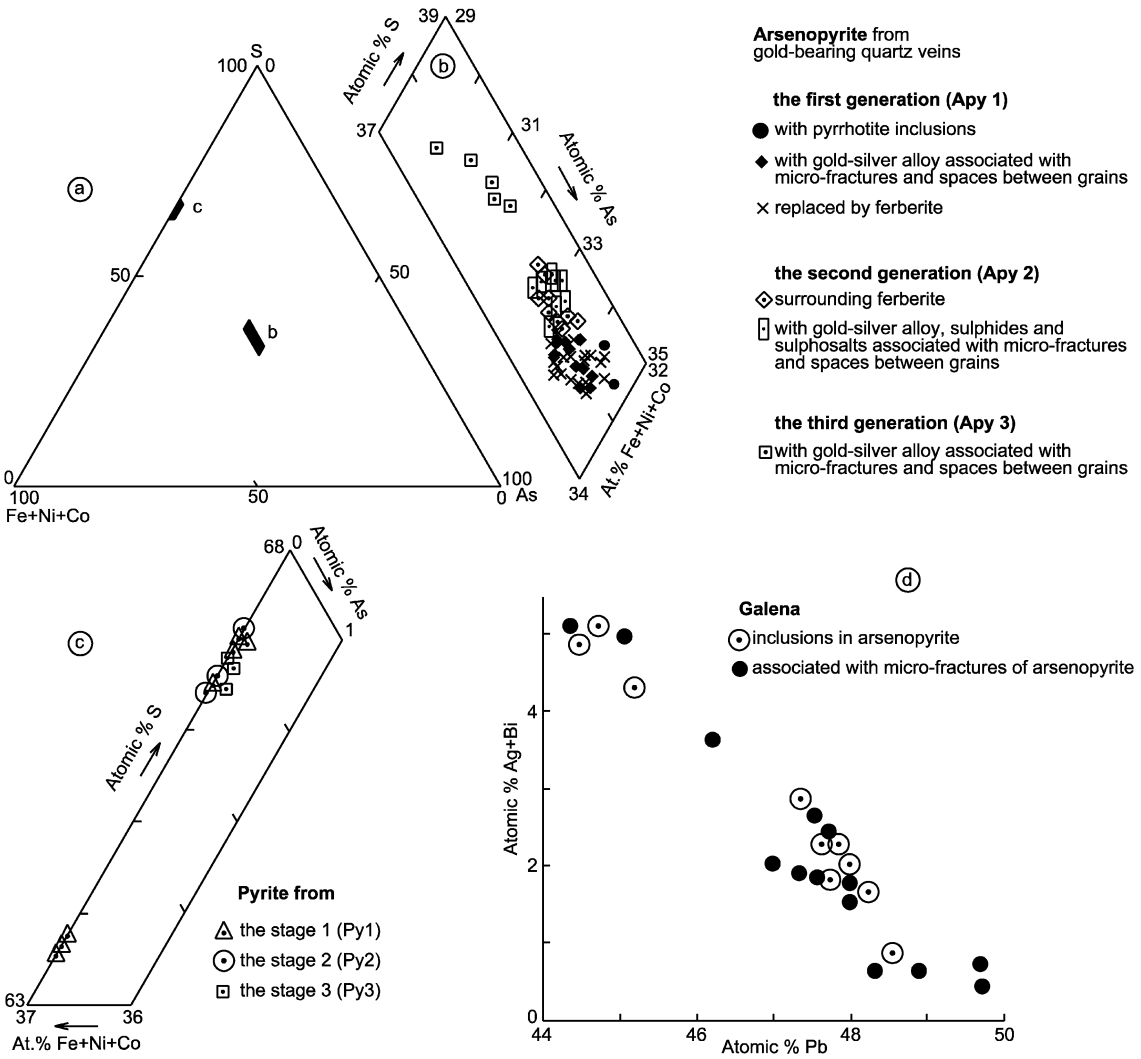

Fig. 6 Compositions of some sulphides from gold-bearing quartz veins of the Santo António mine. **a** S–(Fe + Ni + Co)–As diagram showing the positions of diagrams **b** and **c**; **b** three generations of arsenopyrite are distinguished in the gold-bearing quartz veins; **c** the three pyrite compositions are similar; **d** Ag + Bi versus Pb diagram of galena, suggesting that these metals substitute for Pb in galena

4.3 Stage 3

It has very clear light grey quartz (Qz3) which fills cavities. Arsenopyrite (Apy3) is frequent, anhedral and is fractured. It is As-deficient and S-rich. Very rare crystals of arsenopyrite are zoned with a darker core of Apy2 and a lighter rim of Apy3, showing increase in Fe and S contents and a decrease in the As content from core to rim (Table 2). An increase in the S content and a decrease in the As content of arsenopyrite is observed from the stage 1 to the stage 2 and the stage 3 (Fig. 6b). Pyrite (Py3) is rare, anhedral and occurs as veinlets. Pyrite from the three stages has a similar composition (Table 2, Fig. 6c), but a few compositions of the stage 1 have the lowest S content and the highest Fe + Ni + Co content. Subhedral and anhedral gold–silver alloy (Au–Ag3) occurs associated with micro-fractures and between grains of arsenopyrite (Apy3) (Fig. 5j) and rarely also fills micro-fractures of pyrite (Py3). There is not a distinct chemical composition of gold–silver alloy from the three stages (Fig. 7). Scheelite ($Ca_{0.87}W_{1.04}O_4$) is very rare, anhedral and occurs included in quartz (Qz3). Chalcopyrite, galena and marcasite (FeS_2) are rare, anhedral and surround pyrite (Py3). No distinction was found in the composition of galena (Fig. 6d). It contains up to 2.11 wt% Ag (Table 2) and 5.46 wt% Bi. The Ag is quite insoluble in PbS if Sb or Bi are absent at significant temperatures (Amcoff 1976). This galena does not contain Sb. The coupled substitution of $Bi^{3+} + Ag^{+}$ for $2Pb^{2+}$ is suggested by Fig. 6d and is stable (Amcoff 1976).

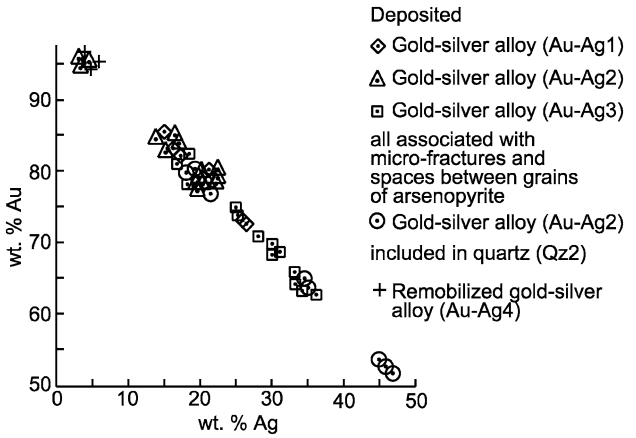

Fig. 7 Compositions of gold and electrum grains from gold-bearing quartz veins of the Santo António mine showing that generally different generations of gold and electrum are not distinct

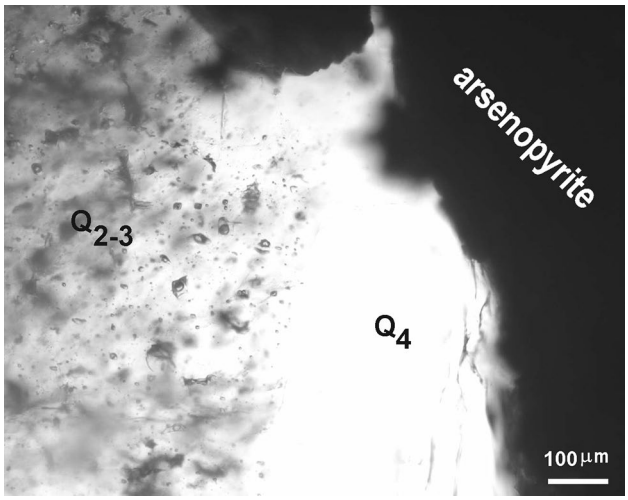

Fig. 8 Spatial relationship between quartz associated with hypogenic stages (2–3) and remobilized quartz (stage 4) and arsenopyrite, from a gold-bearing quartz vein of the Santo António mine

4.4 Late hydrothermal remobilization stage

The late hydrothermal remobilization stage consists mainly of clear quartz (Qz4) which resulted from remobilization of previous quartz, gold–silver alloy (Au–Ag4) (Fig. 5l) with a composition similar to that of the richest Au–Ag2 in Au (Fig. 7) and the occurrence of supergene covellite ($Cu_{0.93}S$). Covellite is rare and partially surrounds arsenopyrite (Apy3) and bismuthinite. All minerals are anhedral.

4.5 Weathering products

Stolzite ($Pb_{1.00}W_{1.00}O_4$) is anhedral, replaces scheelite (Fig. 5k). Rooseveltite ($Bi_{1.09}As_{0.95}O_4$) is anhedral, very rare and partially surrounds arsenopyrite (Apy3), bismuthinite and covellite. Scorodite ($Fe^{3+}_{1.2}As_{1.2}O_{4.2}H_2O$) is subhedral, not frequent and occurs associated with micro-fractures of arsenopyrite (Apy2), gold–silver alloy (Au–Ag4) (Fig. 5l) and bismuthinite.

5 Fluid inclusions

Studies of the types and petrography of fluid inclusions were carried out on wafers from representative samples of three outcropping mineralized quartz veins and one vein underground at the former mine, all in the Santo António mine. The succession of fluids and possible mineralization events has been studied by interpreting the relationships between fluid inclusions and the different quartz types recognized during the petrographic study. We have observed four types of quartz: the older (Q_1) from the hypogene stage 1 is dark with very small fluid inclusions and very often deformed and partly recrystallized. Quartz from the hypogene stages 2 and 3 (Q_2 and Q_3 respectively), are much more clear than Q_1, practically undeformed and the fluid inclusions are much bigger. The last type of quartz (Q_4) from the late hydrothermal remobilization stage is undeformed, very clear, practically without fluid inclusions and often in contact with the main sulphides (Fig. 8). The fluid inclusion studies were performed in quartz Q_2 and Q_3 ($Q_{2–3}$) without distinction because both quartz has identical characteristics when observed on tick sections proper for the fluid inclusion study and also because both has the same fluid inclusion assemblages. They focused on fluid inclusion assemblages composed of groups of inclusions, isolated inclusions or inclusions in trails, all with identical characteristics concerning the vapor/liquid ratio, composition, heating and freezing behavior. The lack of growth zones in the quartz precludes an unambiguous classification as primary inclusions, but according to Roedder's (1984) criteria those in intracrystalline trails and at least some of the isolated inclusions should be pseudosecondary and primary, respectively, coeval with quartz crystallization.

5.1 Fluid characterization

All the studied fluid inclusions are between 5 and 30 µm. We have estimated a density of around 1,500 fluid inclusions bigger than 5 µm in 1 mm^3 of quartz $Q_{2–3}$. From petrographic, microthermometric and Raman characteristics different types of fluids (nomenclature according to Boiron et al. 1992) were recognized (Fig. 9): (1) Lc-w type: aqueous carbonic fluids (H_2O–CO_2–CH_4–N_2–NaCl) triphasic in the range 10–25 °C. The volume fraction of the aqueous phase

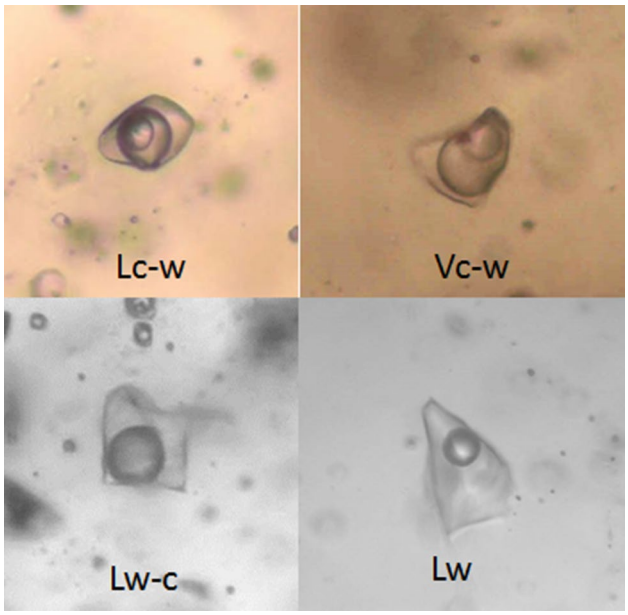

Fig. 9 Fluid inclusion images of the fluid types: Lc-w, Vc-w, Lw-c and Lw from gold-bearing quartz veins of the Santo António mine. See Sect. 5.1 in the text for fluid type characteristics. Inclusions are in the range 15–30 µm

(Flw) is in the range of 0.4–0.6. These are the most obvious fluids in all samples. They could represent more than 50% of the fluid inclusion population. (2) Vc-w type: identical to Lc-w, but with Th_{tot} in vapor as the only difference (3) Lw-c type: aqueous carbonic fluids (H_2O–CO_2–CH_4–N_2–NaCl) always biphasic at room temperature and with the Flw ranging between 0.6 and 0.7. This type of fluids is scattered in the samples. (4) Lw type: low salinity aqueous fluids (H_2O–NaCl), with the Flw around 0.9. This type of fluid can be observed in every sample although they represent probably less than 20% of the fluid inclusions (Fig. 10).

Locally all types can be seen in trails traversing quartz (Q_1), which attest a secondary origin in relation to this quartz generation. The aqueous carbonic fluids were observed in clusters, occasionally isolated and in intragranular trails only in quartz Q_2 associated with sulphides and often placed less than 1 mm from these phases. The Lw fluid type occurs mostly in trails but some are associated with clusters of the aqueous carbonic Lw-c fluids. A summary of the microthermometric characteristics, micro-Raman data and bulk composition, for selected fluid inclusions, is given in Table 4.

5.1.1 Microthermometry and Raman characteristics of the aqueous carbonic fluids

In the Lc-w fluids we could measure the melting temperature of the CO_2-rich phase ($TmCO_2$), the melting of clathrates (Tm_{Cl}), occasionally the temperature of ice melting (Tm_{ice}) and the temperature of gas homogenization ($ThCO_2$). In the Lw-c fluid inclusions, we could only measure Tm_{Cl} and Tm_{ice} (Fig. 11). Many of the Lc-w and Lw-c inclusions decrepitated, and some leaked, during the heating experiments, even at a temperature gradient as low as 1 °C/min due to the high internal pressure. Rarely, we could measure temperatures of total homogenization (Th_{tot}), but often these temperatures could not be observed accurately due to the darkening of the inclusion during heating. $TmCO_2$ was registered between −57.4 and −59.2 °C (average of −58.5 °C), the melting temperature of clathrate was in the range 8.6–10.5 °C (average of 9.6 °C) and the homogenization temperature of CO_2 was observed in the range of 13.0–25.5 °C (to the liquid, average of 20.1 °C) and 11.6–20.0 °C (to the vapour, average of 16.5 °C). Flc (liquid CO_2/total CO_2) near $TmCO_2$ was around 0.50. Th_{tot} in these Lc-w fluid inclusions was between 350 and 386 °C (average of 372 °C) to the liquid phase. The temperature of melting clathrates in the Lw-c fluids were between 8.2 and 11.2 °C (average of 9.5 °C), and the melting of the last ice crystal was in the range −2.0° to −3.0 °C (average of −2.3 °C). Th_{tot} in these Lw-c fluid inclusions ranges between 290° and 320 °C (average of 303 °C) for the liquid phase. A representative set of these

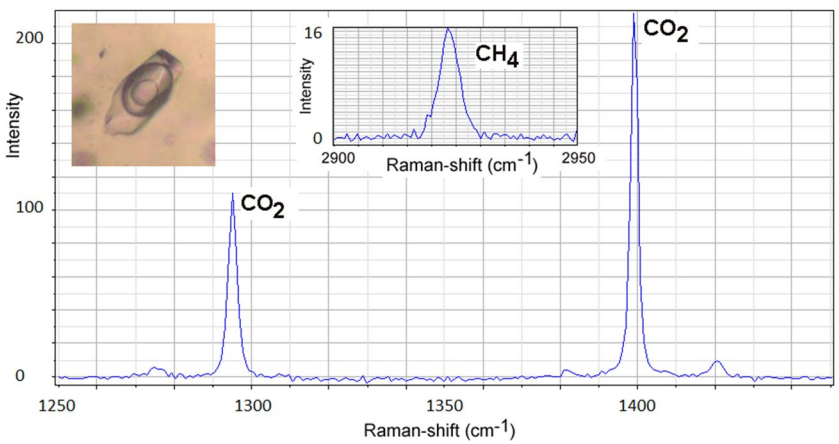

Fig. 10 Raman spectrum on CO_2 lines from a Lc-w fluid inclusion (image inside) of gold-bearing quartz veins from the Santo António mine

Table 4 Microthermometry, gas composition, global composition and densities for selected fluid inclusions of gold-bearing quartz veins from the Santo António mine, Penedono, northern Portugal

F.I.	Flw	FI type	Microthermometry (°C)					Gas composition (%)			Global composition (mol%)						Density
			$TmCO_2$	TmCl	Tm_{ice}	$ThCO_2$	TH	CO_2	CH_4	N_2	H_2O	CO_2	CH_4	N_2	Na^+	Cl^-	
P1-1	60	Lc-w	−58.8	9.8		23.8	L 375	97.87	1.75	0.38	75.62	17.30	0.28	0.06	3.35	3.35	0.85
P1-2	60	Lc-w	−58.8	9.7	−2.0	23.3	L 378	97.58	2.42	nd	75.32	17.36	0.39	0.00	3.46	3.46	0.85
P1-3	60	Lc-w	−59.2	10.0		22.7	L 360	96.84	2.90	0.25	75.82	17.23	0.46	0.04	3.22	3.22	0.85
P2-1	70	Lw-c		11.2	−2.4		>330	82.35	17.65	nd	92.19	4.94	0.54	0.00	1.17	1.17	0.76
P2-2	70	Lw-c		11.0	−2.0		>300	83.58	16.42	nd	92.23	4.91	0.49	0.00	1.18	1.18	0.76
P2-3	60	Lc-w	−59.7	10.5		11.6	V	93.24	6.76	nd	81.93	16.50	1.04	0.00	0.25	0.25	0.85
P6-1	40	Lc-w	−58.9			22.0	L	96.46	2.64	0.90							
P6-2	60	Lc-w	−59.2	9.1		23.6	L	96.22	3.78	nd	74.83	16.97	0.60	0.00	3.80	3.80	0.84
P6-3	40	Lc-w	−58.0	8.6		22.1	V	100	nd	nd	82.88	14.34	0.00	0.00	1.39	1.39	0.52

F.I. fluid inclusion, *Flw* filling water, *$TmCO_2$* temperature of melting of the gas phase, *TmCl* temperature of melting of clathrates, *Tm_{ice}* ice melting temperature, *$ThCO_2$* temperature of gas homogenization, *TH* homogenization temperature

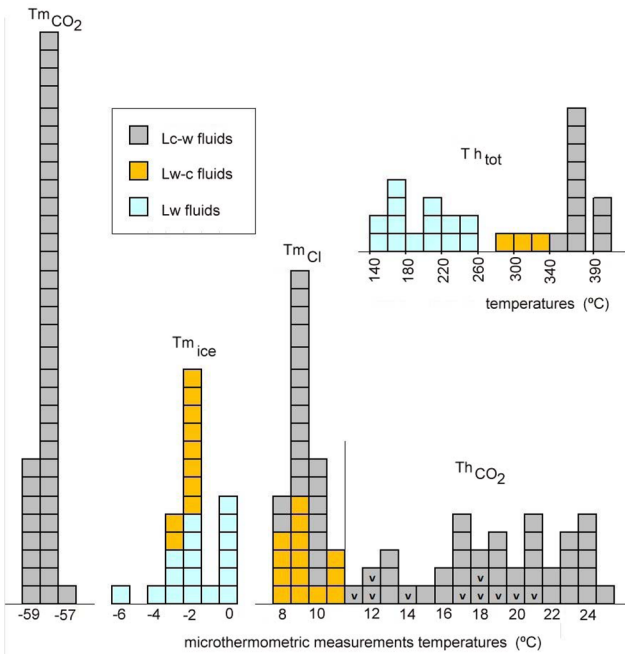

Fig. 11 Microthermometric measurements on fluid inclusions in quartz from Santo António Au–As quartz veins. See text for significance of abbreviations

inclusions was selected for Raman spectroscopy analyses. Carbon dioxide (CO_2), methane (CH_4) and nitrogen (N_2) were the only gaseous species found. The molar content of the gases is dominated by CO_2 which ranged from 82.35 to 100%; CH_4 ranged from 0 to 17.65%; N_2 was detected only in one-third of the inclusion and the highest content was 0.90%. These fluids had the following bulk compositions (%): Lc-w: 74.8–82.9 mol% H_2O, 14.3–17.4 mol% CO_2, up to 1 mol% CH_4, up to 0.06 mol% N_2, and 0.3–3.8 mol % Na^+ and the same for Cl^-. The densities were between 0.52 and 0.85 g cm^{-3}. The Lw-c fluids had the following average composition: 92.2 mol% H_2O, 4.9 mol% CO_2, 0.5 mol% CH_4, no N_2, and 1.2 mol% of both Na^+ and Cl^- (Table 4). Figure 11 shows the CO_2 and CH_4 Raman main peaks for a typical aqueous Lc-w fluid inclusion.

5.1.2 Microthermometry of the aqueous fluids

Ice melting temperatures (Tm_{ice}) of Lw fluid inclusions measured in quartz l are between −7.4 and −0.1 °C (average of −3.4 °C) corresponding to salinities lower than or equal to 9.7 eq. wt% NaCl (average of 3.6 eq. wt% NaCl). Lw inclusions displayed Th_{tot} values in the interval 150–250 °C (average of 195 °C). The densities were between 0.84 and 0.99 g cm^{-3}.

6 Isotopic data

6.1 Sulfur, Helium, Neon and Argon isotopes

It was not possible to separate pyrite or arsenopyrite grains according with their stage in the ore deposition because of the intricate nature of ore textures. The $\delta^{34}S$ values of pyrite and arsenopyrite of four gold quartz veins are presented in Table 5 and Fig. 12. They range between −4.0 and −3.7‰ for pyrite, with a mean value of −3.8‰, and between −5.3 and −4.3‰ for arsenopyrite, with a mean value of −4.7‰.

Isotopic data of He, Ne and Ar from fluid inclusions in pyrite of the gold quartz veins are given in Table 6. The concentrations of ^4He range from 0.53×10^{-7} to 1.40×10^{-7} cm^3 STP/g. Those of ^{22}Ne are of $(0.693–4.31) \times 10^{-11}$ cm^3 STP/g and those of ^{36}Ar are of

Table 5 $\delta^{34}S$ sulphide data of pyrite and arsenopyrite of gold-bearing quartz veins from the Santo António mine, Penedono, northern Portugal

Sample reference	$\delta^{34}S$ ‰ pyrite	Sample number	$\delta^{34}S$ ‰ arsenopyrite
P1	−3.9	A1	−4.6
P2	−4.0	A2	−4.3
P3	−3.8	A3	−4.8
P4	−3.6	A4	−4.3
P5	−3.8	A5	−5.0
P6	−3.7	A6	−5.3

Precision and reproducibility $\delta^{34}S$ were better than 0.2‰

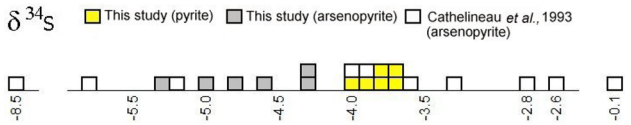

Fig. 12 Sulphur isotopic data ($\delta^{34}S$) from pyrite and arsenopyrite from four gold-bearing quartz veins from the Santo António mine, Penedono, and literature

$(0.191–1.01) \times 10^{-9}$ cm^3 STP/g. Noble gas ratios are R/Ra of 0.126–0.201 (for He, where R = sample $^3He/^4He$, Ra = air $^3He/^4He$), $^{20}Ne/^{22}Ne$ of 9.80–9.87, $^{21}Ne/^{22}Ne$ of 0.0294–0.0302, $^{38}Ar/^{36}Ar$ of 0.1864–0.1884 and $^{40}Ar/^{36}Ar$ of 298.1–324.8.

6.2 U–Pb Geochronology of the Tabuaço Massif

The Tabuaço Massif hosting the Santo António deposit has now been dated for the first time. Monazite in the granite sample yields a $^{207}Pb/^{235}U$ age of 310.1 ± 1.1 Ma (Table 7, Fig. 13). Coexisting zircon is extremely rich in U (1000-10000 ppm) and three analyses yield variously discordant data defining an upper intercept age of 306.3 ± 1.8 Ma, which is broadly consistent with the monazite age.

7 Discussion

7.1 Mineralogy

The mineral paragenesis for gold-bearing quartz veins from Santo António (Table 1) differs from that of Sousa and Ramos (1991) and Leal Gomes (2000b), because it includes more minerals.

In the gold-bearing quartz veins from Santo António, arsenopyrite is the most abundant sulphide and the only one that shows distinct compositions. There is a progressive increase in the S content and decrease in the As content from

Table 6 He–Ar–Ne isotopic compositions of inclusion-trapped fluid in pyrite of gold-bearing quartz veins from the Santo António mine, Penedono, northern Portugal

Pyrite	Weight (g)	^4He	R/Ra	1 s	$^{40}Ar/^{36}Ar$	1 s	^{36}Ar	$^{38}Ar/^{36}Ar$	1 s	^{22}Ne	$^{20}Ne/^{22}Ne$	1s	$^{21}Ne/^{22}Ne$	1s
3	1.02	5.26E−08	0.126	0.008	306.6	4.10	2.26E−10	0.1881	0.0006	6.98E−10	9.80	0.06	0.0294	0.0004
5	1.00	8.01E−08	0.136	0.007	324.8	4.40	1.91E−10	0.1884	0.0005	6.93E−10	9.81	0.06	0.0300	0.0004
4	1.00	1.05E−07	0.177	0.007	298.7	4.00	5.78E−10	0.1878	0.0006	2.10E−11	9.80	0.06	0.0296	0.0004
6	1.02	1.40E−07	0.201	0.005	303.3	4.10	1.01E−09	0.1875	0.0005	4.31E−11	9.87	0.06	0.0296	0.0004
1	1.02	7.35E−08	0.142	0.007	311.6	4.20	2.90E−10	0.1864	0.0005	1.10E−11	9.83	0.06	0.0301	0.0004
2	1.02	8.02E−08	0.142	0.007	313.4	4.20	2.18E−10	0.1878	0.0006	7.21E−12	9.81	0.06	0.0302	0.0005
7	1.01	5.89E−08	0.131	0.007	298.1	4.00	5.42E−10	0.1740	0.0007	1.91E−11	9.81	0.06	0.0295	0.0004
Air			1.000		295.5			0.1880			9.80		0.0290	

Units of concentrations are cm^3STP/g

Table 7 U-Pb data for zircon and monazite in granite from Santo António

Mineral characteristics[a]	Weight[b] [µg]	U[b] [ppm]	Th/U[c]	Pbi[d] [ppm]	Pbc[e] [pg]	$^{206}Pb/^{204}Pb$[f]	$^{207}Pb/^{235}U$[g]	± 2σ [abs]	$^{206}Pb/^{238}U$[g]	± 2σ [abs]	rho	$^{207}Pb/^{206}Pb$[g]	± 2σ	$^{206}Pb/^{238}U$[g] [Ma]	± 2σ	$^{207}Pb/^{235}U$[g]	± 2σ	$^{207}Pb/^{206}Pb$[g]	± 2σ	Disc [%]
P3.7 - granite Penedono area																				
M NA [1]	1	2437	6.26	4.84	6.8	1127	0.3575	0.0015	0.04951	0.00010	0.62	0.05238	0.00017	311.5	0.6	310.4	1.1	301.9	7.3	-3.3
Z lp AA [1]	1	8822	0.01	0.01	2.0	12425	0.3292	0.0010	0.04546	0.00011	0.92	0.05251	0.00006	286.6	0.7	288.9	0.7	307.7	2.6	7.0
Z AA [1]	1	9082	0.01	0.00	2.0	13076	0.3287	0.0009	0.04543	0.00010	0.92	0.05247	0.00006	286.4	0.6	288.5	0.7	305.8	2.5	6.5
Z fr AA [1]	1	1125	0.13	0.00	1.3	362	0.0451	0.0009	0.00614	0.00002	0.46	0.05326	0.00103	39	0	45	1	340	43	89

[a] Z = zircon; M = monazite; fr = fragment; lp = long prismtic (l/w > 5); AA = treated with air abrasion; NA = not abraded; [1] = number of grains

[b] weights and concentrations know to about 50%

[c] Th/U model ratio inferred from 208/206 ratio and age of sample

[d] Pbi = initial common Pb (corrected for blank)

[e] Pbc = total common Pb in sample (initial + blank)

[f] raw data corrected for fractionation

[g] corrected for fractionation, spike, blank, and initial common Pb; error calculated by propagating the main sources of uncertainty. Initial common Pb corrected with compositions calculated with Stacey and Kramers (1975) model. Decay constants are from Jaffey et al. (1971)

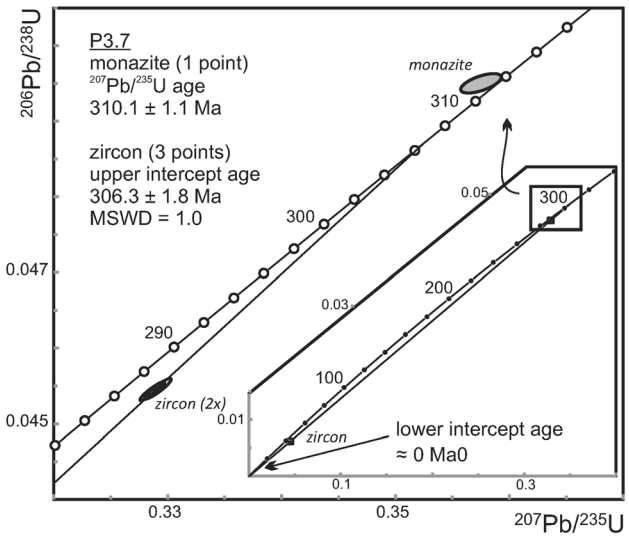

Fig. 13 U–Pb Concordia diagram for monazite and zircon from granite hosting the Santo António mineralization. Ellipse represents 2σ uncertainty

the first generation (Apy1) to the second generation (Apy2) and third generation (Apy3) due to later growths (Fig. 6b). A few crystals of arsenopyrite are zoned with a darker core of Apy2 and a lighter rim of Apy3. Some authors (e.g. Morey et al. 2008; Cook et al. 2013) consider that the zoned crystals of arsenopyrite have alteration rims. Fuertes-Fuente et al. (2016) accept that idea for some crystals, but also admit the growth of a later arsenopyrite for other rims. The preserved zoned crystals suggest that there was no significant sulphide recrystallization (Craig et al. 1993).

As Ni and Co are only up to 0.06 wt% and Sb was not detected in arsenopyrite (Sundlab et al., 1984) from gold-bearing quartz veins of Santo António, the arsenopyrite geothermometer of Kretschmar and Scott (1976) and Sharp et al. (1985) can be applied. Temperatures are estimated for arsenopyrite in equilibrium with pyrite. No arsenopyrite standard was used, and the AsGa standard used may have increased the As content of our data as As is bonded differently than in arsenopyrite. Therefore, the mean and minimum values of at. % As of the three generations of unzoned arsenopyrite and of a selected rare zoned crystal were used avoiding rare values above 34.3 at.% As of the first generation of arsenopyrite as indicated by Kretschmar and Scott (1976). The temperature of unzoned arsenopyrite decreases progressively from Apy1 (444–433 °C) to Apy2 (395–369 °C) and Apy3 (364–300 °C). The zoned arsenopyrite presents a decrease in temperature from core (383–376 °C) to rim (363–329 °C). The temperatures of core and rim are within the ranges of temperatures for Apy2 and Apy3, respectively. The composition of arsenopyrite shows

an increase in the S content and decrease in the As content (Fig. 6b) as the temperature drops.

Experimental data suggest that galenobismutite has a lower stability limit between 390 and 375 °C (Chang and Hoda 1977). Galenobismutite and bismuthinite from the gold-bearing quartz veins of Santo António belong to the stage 2 (Table 1) and the estimated temperatures of 395–369 °C obtained from the Apy2 are in accordance with the experimental temperatures for galenobismutite and bismuthinite.

In the gold-bearing quartz veins from Santo António, three generations of gold–silver alloy (Au–Ag) were distinguished associated with micro-fractures and filling spaces between grains of Apy1, Apy2 and Apy3, respectively (Table 1, Fig. 5a, c, j). Rare Au–Ag2, also occurs included in quartz Qz2 (Fig. 5d). In general, there is no significant distinction in the composition of deposited gold–silver alloy of the three generations (Fig. 7).

7.2 Fluid inclusion studies

The densest aqueous carbonic fluids are H_2O–CO_2 low salinity dominant fluids with only up to 1% mol CH_4 and occasional traces of N_2 (Table 4). Their relatively uniform Flw ratio suggests that the fluid was homogeneous during the entrapment (Fig. 14). This happened at a minimum temperature around 360–380 °C and a pressure ≥ 170 MPa (minimum PT values of the highest isochore at Th_{tot}), and most probably in a lithostatic pressure gradient, which means that the crystallization of quartz from this fluid was at about 7 km depth. The difficulty in obtaining homogenization temperatures in this type of fluid is a common problem (Bodnar et al. 2014). Marcoux et al. (2015) studied very similar fluids and could only measure six Th_{tot}, all homogenized in vapor. The next abundant aqueous carbonic fluid is much more water-rich and although the CH_4/CO_2 ratio is higher than in the previous fluid, it has much less CO_2 and CH_4. This fluid has slightly lower Th_{tot} than the previous fluid, but the most striking characteristic is the much lower pressure around Th_{tot}. The last fluid is aqueous and low salinity, most probably meteoric water that percolated the lithologies above the deposition site. The fact that this Lw-c fluid has a higher ratio of CH_4/CO_2 than the Lc-w fluid could indicate that the fluid percolated through C-rich metasedimentary rocks, lithologies that are relatively abundant in the area. The existence of aqueous carbonic fluids of different densities (Lc-w, Vc-w and Lw-c fluid types) very close (some micra) each other suggest that one of the causes for ore deposition was probably pressure drop possibly triggered by seismic events, a mechanism first proposed by Sibson (1973, 1983, 1987, 1990) and Sibson et al. (1975). Destabilization of the ore forming-fluid due to mixing between aqueous carbonic and water-rich fluids could also have contributed to metallic phase deposition.

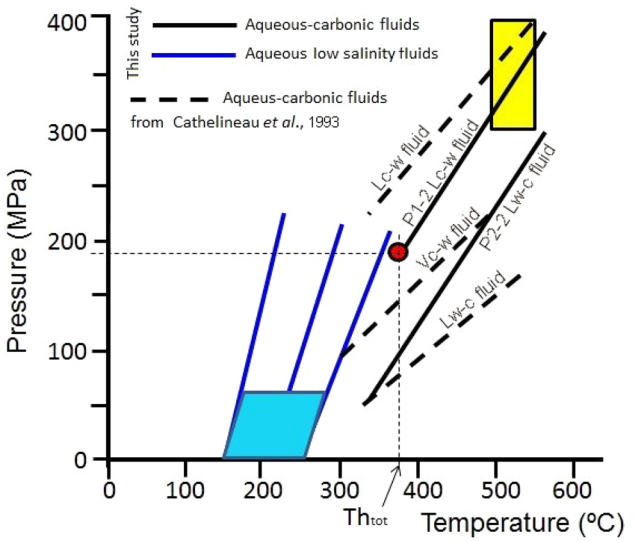

Fig. 14 Isochores for the fluids entrapped in quartz from the Santo António mine orebody and probable PT path for the ore-forming hydrothermal fluid. Yellow area: PT domain constrained by Boiron et al. (1996) for highest PT conditions in the beginning of fluid trapping in mineralized quartz at Penedono and other areas in northwestern Iberia. Red dot: PT point for the aqueous carbonic fluid represented by the isochore (P1-2, see Table 4) fluid at Th_{tot} = 378 °C, which is the lowest temperature (and pressure) for the Lc-w fluid entrapment. This corresponds to ~ 7 km depth, assuming a lithostatic pressure gradient and rock density of 2.7. Blue area: PT domain for the entrapment of water low salinity fluids without measurable gas, considering the lower and the higher isochores (represented also the average isochore) and 7 km at hydrostatic as maximum depth. (Vc-w fluid is an aqueous carbonic fluid with gas homogenization in vapour). Green arrows: probable PT path for the mineralizing fluid at the Santo António mine

In multidisciplinary studies of various gold deposits from the Iberian Peninsula Cathelineau et al. (1993) and Boiron et al. (1996) presented the first data on fluid inclusions from the Penedono area. They describe only three types of H_2O–CO_2–CH_4–N_2–NaCl ± H_2S fluids for this deposit, which they distinguished according to the degree of filling (not quantified), microthermometric and Raman results and accordingly bulk compositions and densities. All the fluids are of low salinity. These authors and also Nogueira and Noronha (1993) do not describe water-(salt) inclusions in this deposit. The aqueous carbonic characteristics are broadly similar to those observed in the present study. These authors considered that the mineralization has evolved from P–T conditions around 370 °C/1–1.5 kbar to 200° ± 20 °C and 0.5 kbar, with gold precipitation occurring during or after this last stage of fluid circulation.

The types of fluids, fluid compositions (gas content and low salinity), densities and temperatures and pressures (and depths) of entrapment are in accordance with an orogenic

type deposit. According to Goldfarb et al. (2005) fluids that form orogenic gold deposits could have been extracted at depths of up to 20 km and percolated through crustal fault zones.

7.3 Isotopic studies

7.3.1 Pyrite and arsenopyrite sulphide data

The Santo António fluid was not dominated by H_2S, which has not been detected by Raman spectroscopic analysis of the studied fluid in quartz. Given the reducing environment in the deposit, sulphur should most probably have been present mainly as HS^- and S^{2-}. Sulphur isotope compositions of hydrothermal S-bearing minerals is controlled by the total sulphur isotope composition of the fluids, temperature, pH and fO_2.

The first parameter is a characteristic of the source, but the latter parameter is related to the environment of deposition (Arias et al. 1997). The $\delta^{34}S$ from sulphides should be equivalent to $\delta^{34}S$ of the ore-forming fluids. The arsenopyrite shows lower $\delta^{34}S$ values than pyrite, as found in orogenic gold deposits of Mali, West Africa (Lawrence et al. 2013b). The $\delta^{34}S$ mean values of −3.8‰ for pyrite and −4.7‰ for the arsenopyrite of the Santo António deposit can be compared to the total range of published data extending for −0.1 to −8.5 of arsenopyrite (Fig. 12; Cathelineau et al. 1993) for orogenic gold veins of Penedono in Portugal and Corcoesto, Tomino and Pino in Spain. The sulphur isotopic composition of arsenopyrite and pyrite from the Au Limarinho deposit are only slightly negative then the average S isotopic composition from Penedono main sulphides. Values close to 0‰ for $\delta^{34}S$ have been interpreted as being indicative of a magmatic fluid (Ohmoto and Goldhaber 1997), although according to a compilation of European granites $\delta^{34}S$ in magmatic systems could range from +9 to −4‰ (Gunter 1986). The $\delta^{34}S$ values obtained in the Santo António mining area are within the range for those found in orogenic gold deposits from the Juneau gold belt of southeastern Alaska (−17.8‰ to 1.2‰; Goldfarb et al. 1991), but they are constrained to a much more narrow range of −3.7‰ to −5.3‰ (Fig. 15) suggesting that most of the fluid acquired its sulphur signature from a country rock of relatively homogeneous chemistry. However, some orogenic gold deposits from NW Spain hosted by Cambrian–Ordovician or Ordovician rocks present positive $\delta^{34}S$ values of sulphides from +9.7 to +20.6‰ in the Navia Belt (Arias et al. 1997), from +3.2 to +18.0‰ in the Southern West Asturian Leonese zone (Tornos et al. 1997) and from +6.8 to +19.5‰ in the Llamas de Cabrera area (Gómez-Fernández et al. 2012), which are similar to those in the respective host metasedimentary rocks.

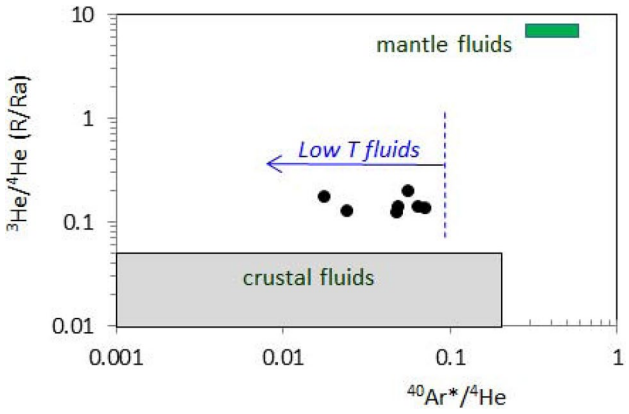

Fig. 15 $^{40}Ar^*/^4He$ vs. $^3He/^4He$ (R/Ra) diagram for fluids liberated from pyrites from gold-bearing quartz veins of the Santo António mine. Small rectangle delimits lithospheric subcontinental mantle values. $^{40}Ar^*$ is non-atmospheric argon, i.e. $^{40}Ar^* = {}^{40}Ar - 295.5\ {}^{36}Ar$

7.3.2 Helium–argon–neon isotopic data from fluids in pyrite

Helium and argon isotopic data are important for tracing ore-forming fluids, namely to distinguish those coming from the mantle and also to separate meteoric from crustal generated fluids.

Since Simmons et al. (1987), it is accepted that hydrothermal minerals can preserve mantle derived ^3He. The other helium isotope (^4He) is considered always radiogenic (produced by the alpha decay of U and Th) and so the atmospheric contribution of ^4He is negligible. These authors also concluded that the $^3He/^4He$ ratio (R) in the crust is < 10% the atmospheric $^3He/^4He$ ratio (Ra) and mantle R/Ra is ~8–9, although subcontinental mantle has R ~ 6. Further studies concluded that in many circumstances the R/Ra of mantle fluids is 1000 higher than in crustal fluids. Many studies (e.g. Simmons et al. 1987; Kendrick et al. 2011) have established that pyrite traps helium over geological time scales (up to 10^9 years). Sample contaminations from cosmogenic ^3He (and ^{21}Ne) are only significant if they have been exposed to the surface for periods of more than a few thousand years (Ozima and Podosek 2002); this problem does not apply to our study because samples used in noble gas analysis have been collected underground in the mine. The noble gas data seem valid, because although there are different fluid generations in the samples, the aqueous carbonic fluids (the deeper fluids) are much more abundant than the aqueous fluid.

Helium as a geological resource is obtained from He-rich natural gas fields (although He and methane have different genesis) and so the source area is probably the same for both gases. However, He isotopes are used to determine if mantle fluid has contributed (in some extent) to the fluid.

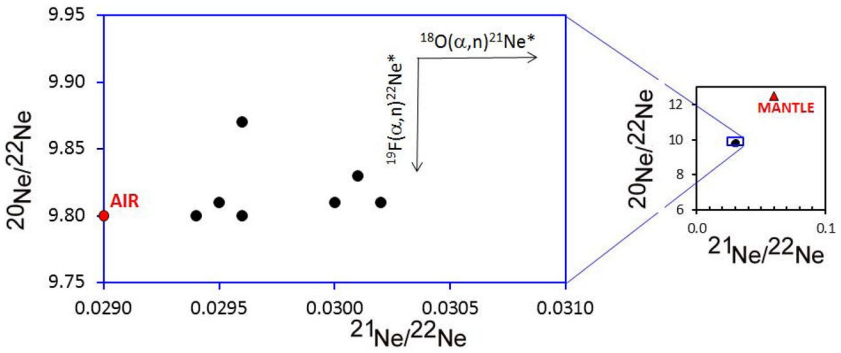

Fig. 16 Neon isotopic data for fluids trapped in pyrites from gold-bearing quartz veins from the Santo António mine, Penedono. Radiogenic ^{21}Ne and ^{22}Ne are produced by alpha particles interacting with ^{18}O or ^{19}F, respectively. The displacement of $^{21}Ne/^{22}Ne$ from AIR neon ratio probably reflects mixing of the distinct basement signature with atmospheric noble gases present either in ground water or metasediments (Kendrick and Burnard 2013)

The recent determination of $^{40}Ar/^{36}Ar$ in modern air is 299 (Lee et al. 2006; Valkiers et al. 2010). Meteoric water is characterized by atmospheric noble gas signatures of $^{20}Ne/^{22}Ne < 9.8$ and $^{21}Ne/^{22}Ne > 0.029$, but $^{40}Ar/^{36}Ar$ can range from 299 to 100,000 (Kendrick and Burnard 2013). Radiogenic noble gas isotopes have predictable ratios (e.g. $^{4}He/^{40}Ar^{*}$, $^{21}Ne^{*}/^{40}Ar^{*}$) controlled by the (U + Th)/K ratio of the host rock (asterisk denote radiogenic noble gas isotopes corrected for atmospheric contributions). $^{20}Ne/^{36}Ar$ is 0.524 in air and 0.122 in meteoric waters, but can vary between 0.05 and 6 in shales and between 0.2 and 6.5 in crystalline basement. Smaller components of mantle derived noble gas can be identified from $^{3}He/^{4}He > 0.1$ Ra and elevated $^{3}He/^{36}Ar$ (Kendrick and Burnard 2013). Several orogenic-gold deposits from many parts of the world have maximum fluid inclusion $^{3}He/^{4}He$ ratios of less than 0.4 Ra (e.g. Pettke et al. 1997; Graupner et al. 2006, 2010). Kendrick et al. (2001) proposed the following expression to estimate the amount of fluid from the mantle: $He_{mantle}(\%) = [Ra_{sample} - Ra_{crust}]/[Ra_{mantle} - Ra_{crust}] \times 100$. Assuming $Ra_{mantle} = 6$ and $Ra_{crust} = 0.02$ (Stuart et al. 1995; Zhai et al. 2012), the highest mantle contribution to the ore-forming fluids at the Santo António mine is 2.8%. The well-known natural CO_2 gas field at McElmo Dome (USA) has a $^{3}He/^{4}He$ ratio of 0.13–0.17 which was interpreted by Gilfillan et al. (2008) as a demonstration of a potential small mantle helium component in the gas field. The maximum value of $^{40}Ar/^{36}Ar = 324.8$ could imply that 10% of the fluid probably is of meteoric origin. The contribution of a low temperature meteoric fluid is also suggested by the shift to the left in the diagram of Fig. 16. A small fluid amount escaped from the sub continental lithospheric mantle and incorporated in the ore-forming fluid is consistent with our He–Ar isotopic data and also bulk fluid compositions obtained in the fluid inclusion study. The amount of meteoric water percolation is consistent with the noble gas results and agrees very well with the fluid inclusion data. Neon isotopic ratios also suggest that a fluid contribution from the mantle is absent or very small (Fig. 16). Therefore, the fluids have a dominant crustal origin.

7.4 Mineralizing environment and source of ore metals and metalloids

Gold-bearing quartz veins from the Santo António mine are hosted by the Tabuaço Massif (Fig. 2), which consists of a syn-D3 muscovite > biotite S-type granite dated at 310.1 ± 1.1 Ma (Fig. 13). This granite intruded Cambrian metamorphic rocks and the D_2 extensional shear zone (Figs. 1c and 2) that reached amphibolite-facies metamorphic conditions. The gold-bearing quartz veins fill dilatation surfaces of this granite formed in relation to the motion of D_3 strike-slip shear zones. Therefore, the Tabuaço granite and associated gold-bearing quartz veins are post- M_2 high-grade metamorphism (Fig. 1d). The peak of M_2 metamorphism probably occurred between ca. 320 and 314 Ma (Fig. 1d). The metamorphic conditions estimated on calc-silicate rocks interlayered with the metapelites of the anatectic complex provided minimum metamorphic peak conditions of T = 761 ± 50 °C and P = 5.0 ± 1.0 kbar, but petrological modelling results show that temperature conditions may have exceeded 800 °C (Pereira et al. 2017). Therefore, the studied gold-bearing quartz veins are post- M2 metamorphic peak like many other occurrences in western Europe (e.g. Boiron et al. 1996, 2001; Noronha et al. 2000; Gómez-Fernández et al. 2012; Fuertes-Fuente et al. 2016).

In the Penedono mining area, an earlier major heat sink with steep metamorphic gradients was probably related to development of the D_2 extensional Pinhel shear zone (Díez Fernández and Pereira 2016). The Tabuaço granite hosting the gold-bearing quartz veins from Santo António is younger than the M_2 metamorphic peak between ca. 320

and 314 Ma (Fig. 1d). Therefore, the ascent of the granitic magma would have provided much heat and remobilized gold and other metals and metalloids from the metamorphic rocks in a similar way as recognized in other gold deposits in northwest Europe (e.g. Noronha et al. 2000; Boiron et al. 2003; Vallance et al. 2003). There were two main reservoirs for the mineralized fluids that generated this type of gold deposits. One reservoir consisted of waters percolated into the basement through faults enhanced by shear zones and decompression, equilibrated with metamorphic rocks, transporting dissolved gold, other metals and metalloids which later flowed upwards along the faults. Gold precipitation was probably linked to dilution by fluid mixing during the basement uplift as temperature and pressure drop, as proposed to explain several gold quartz veins from northwest Europe (e.g. Boiron et al. 1996, 2001, 2003; Noronha et al. 2000; Vallance et al. 2003; Gómez-Fernández et al. 2012). Sudden pressure drops caused by seismic events, a mechanism first proposed by Sibson (1973, 1983, 1987, 1990) and Sibson et al. (1975) could also contribute to gold precipitation. The presence of microfractured sulphides could have enhanced gold precipitation through electrochemical processes (Boiron et al. 2003). Tungsten may have been leached from the country rocks in a manner similar to that documented by Cave et al. (2017).

In hydrothermal systems, gold transport and deposition depends on fluid composition, temperature, pressure, pH, oxygen and sulphur fugacity, and type and amount of dissolved sulphur and other species (e.g. Mikucki 1998). The occurrences of several sulphides and sulphosalts, gold–silver alloy from gold-bearing quartz veins of the Santo António mining camp suggest that Au and Ag were carried as bisulphide complexes. The host Tabuaço granite was hydrothermally altered at quartz vein walls and contains secondary muscovite. Neutral to slightly alkaline solutions originating in the field of maximum gold solubility as a bisulphide complex produce sericite as the most common potassium aluminosilicate in alteration assemblages (Romberger 1986). Gold and silver were probably transported as $Au(HS)_2^-$ and $Ag(HS)_2^-$, respectively, under neutral pH conditions (Stefánsson and Seward 2003, 2004; Pokrovski et al. 2014). The decrease in temperature from 444 to 300 °C estimated through the evolution of arsenopyrite composition, including the range of 380–360 °C recorded in fluid inclusions, and the decrease in pressure provided favorable conditions for the gold deposition.

7.5 Comparison with some other gold deposits in the Iberian Massif

In order to compare the Variscan gold deposit from Santo António, Penedono, NW Portugal, with some Variscan gold deposits in the Iberian Massif, we selected data from the literature from northwest to central Iberia (Table 8). All gold deposits occur in shear zones and most of them consist of arsenopyrite-gold quartz veins. However, antimony-gold quartz veins occur in the Central Iberian Zone, and in central Portugal and central Spain. Arsenopyrite-gold quartz veins are mainly hosted by granite, as in the Santo António mine and also the Limarinho deposit, or by granites and metasedimentary rocks, or less commonly by metasedimentary rocks. Antimony-gold quartz veins are hosted by metasedimentary rocks as in the Dúrico-Beirão Mining District. All gold deposits contain sulphides and most of them, as in the Santo António mine, also have sulphosalts. However, rare ferberite occurs in gold-bearing quartz veins from Santo António, but it does not occur in the other selected gold deposits from the Iberian Massif (Table 8). In all selected arsenopyrite-gold quartz veins there were at least two types of fluids, an aqueous-carbonic fluid and an aqueous fluid. Both fluids mixed inside the faults with decrease in temperature and pressure during the basement uplift. This probably caused deposition of gold–silver alloy in these gold-bearing quartz veins (Table 8).

The $\delta^{34}S$ presents negative values in arsenopyrite-gold quartz veins from Santo António and Limarinho deposits, in N Portugal, and positive values in similar veins from Llamas de Cabrera, in NW Spain (Table 8). The $\delta^{34}S$ values will depend on those of metasedimentary rocks from the respective area, as suggested by values in the Llamas de Cabrera deposit. Isotopic He, Ar and Ne values are only available for arsenopyrite-gold-bearing quartz veins from the Santo António mine and suggest a crustal origin. These veins were formed at a depth of 7 km, which is within the range of 6–12 km for most of the selected arsenopyrite-gold quartz veins (e.g. Gómez-Fernández et al. 2012). Considering the three most important reservoirs for sulphur [magmatic, marine and (meta)sedimentary] the $d^{34}S$ values for the studied sulphides at Santo António are compatible only with a metasedimentary source, which in turn strongly suggests that the sulphides belong to an orogenic gold deposit.

The arsenopyrite-gold bearing quartz veins from the Santo António mine compare well with other similar Variscan arsenopyrite-gold quartz veins from the Iberian Massif (Table 8), but these deposits do not contain ferberite. However, there are some differences when compared with the antimony-gold quartz veins: they do not contain antimony minerals, but have rare ferberite and are formed at higher pressure.

Table 8 Selected Variscan orogenic gold deposits in the Iberian Massif

Deposit/Au district	Main type of ore	Host rock	Paragenesis	Fluid composition and P–T conditions	$\delta^{34}S$ per mil	Other characteristics	References
Santo António, Penedono (Portugal)	Arsenopyrite–gold–quartz veins	Granite	Arsenopyrite–pyrite–gold–sulphides–sulphosalts	H_2O–CO_2–CH_4–N_2–NaCl 360–380 °C, > 170 MPa	−5.3 to −4.3‰ (arsenopyrite)	Gold precipitated due to mixing between aqueous carbonic and water-rich fluids during transition of a lithostatic pressure gradient to an hydrostatic one He–Ar–Ne data*	This study
				H_2O–NaCl	−4.0 to −3.7‰ (pyrite)		
Grovelas, Penedono, Vila Pouca, Três Minas (Portugal)	Arsenopyrite–gold–quartz veins	Granites Metasedimentary rocks	Arsenopyrite–pyrite–gold–sulphides	H_2O–CO_2–CH_4–NaCl–(H_2S) 300–550 °C, 100–350 MPa	No data	Gold precipitated from meteoric waters, after being remobilized from meta-sediments by aqueous–carbonic fluids	Noronha et al. (2000)
				H_2O–NaCl < 300 °C, < 100 MPa			
Penedono (Portugal), Corcoesto, Tomino, Pino (Spain)	Arsenopyrite–gold–quartz veins	Granites Granites and metamorphic rocks	Arsenopyrite–pyrite–gold–sulphides–sulphosalts	CO_2–CH_4–H_2O–(N_2–H_2S)–NaCl, 450 °C, 150–300 MPa	−8.5 to −0.1‰ (arsenopyrite)	Gold precipitation linked to extended fluid penetration downward in the crust. Crush-leach data	Boiron et al. (1996) and Cathelineau et al. (1993)
				H_2O–NaCl* 260–310 °C, < 75 MPa			
Castromil, Paredes (Portugal)	Arsenopyrite–gold–quartz veins	Granite, contact Metasedimentary Rocks and aplite	Arsenopyrite–pyrite–gold–sulphides	H_2O–CO_2–CH_4–NaCl 400–500 °C, 100–200 MPa	No data	Gold precipitation linked to mixing between two distinct aqueous fluids of contrasting salinity $\delta^{18}O$ data	Vallance et al. (2003)
				H_2O–NaCl, 150–180 °C			
Limarinho (Portugal)	Arsenopyrite–gold–quartz veins	Granite	Arsenopyrite–pyrite–gold–sulphides–sulphosalts	H_2O–CO_2(CH_4–N_2)–NaCl 300–330 °C, 130–200 MPa	−9.2 to −7.1‰ (arsenopyrite) + 1.6‰ (pyrite)	Evolution from aqueous carbonic fluids towards water-richer volatile poorer fluids, that mixed $\delta^{18}O$ δD data	Fuertes-Fuente et al. (2016)
				H_2O–NaCl 285–330 °C, 24–29 MPa			

Table 8 (continued)

Deposit/Au district	Main type of ore	Host rock	Paragenesis	Fluid composition and P–T conditions	$\delta^{34}S$ per mil	Other characteristics	References
Lamas de Cabrera (Spain)	Arsenopyrite–gold–quartz veins	Granites and metasedimentary rocks	Arsenopyrite–pyrite–gold–sulphides	CO_2–(CH_4) H_2O–CO_2–CH_4–N_2–NaCl 300–390 °C, 200–220 MPa H_2O–NaCl 180–310 °C, < 200 MPa	+6.8 to +19.5‰	Gold precipitation linked to decreasing of Au solubility due to mixing between two distinct aqueous fluids $\delta^{18}O$ data	Gómez-Fernández et al. (2012)
Dúrico-Beirã region (Portugal)	Antimony–gold–quartz veins	Metasedimentary rocks	Arsenopyrite–pyrite–berthierite–stibnite–gold–sulphides–sulphosalts	H_2O–NaCl–CO_2(–CH_4) 290–340 °C, no P data H_2O–NaCl 128–225 °C, no P data	No data	Stibnite precipitation due to mixing of an aqueous carbonic fluid with a meteoric one. Pb isotope data indicate a homogeneous lead source of crustal origin	Couto et al. (1990) Neiva et al. (2008)
Central Portugal and Central Iberian regions	Antimony–gold–quartz veins	Metasedimentary rocks	Arsenopyrite–pyrite–stibnite–gold–sulphides–sulphosalts	H_2O(–NaCl)–CO_2–CH_4(–N_2) 300 °C, 150 MPa H_2O–NaCl 128–225 °C, no P data	No data	Gold precipitated in structural setting from unmixing due to pressure release	Dee and Roberts (1993), Ortega and Vindel (1995) and Murphy and Roberts (1997)

*At Penedono authors do not describe this type of fluid

8 Conclusions

1. The gold-bearing quartz veins from the Santo António mine (Penedono, Portugal) cut a deformed Variscan S-type muscovite > biotite granite dated at 310.1 ± 1.1 Ma and are structurally controlled by sinistral sense of motion of N130–140E trending D_3 and N50E trending D_4 strike-slip shear zones. These gold mineralizations are post- M_2 metamorphic peak.

2. Pyrrhotite, arsenopyrite and pyrite are the earliest sulphides. From the first generation to the second and third generations of arsenopyrite, due to later growths, there is a progressive increase in the S content and decrease in the As content and temperature from 444–433 °C to 395–369 °C and 364–300 °C, respectively. In a few single crystals, the S content increases and As content and temperature decrease from core (383–376 °C) to rim (363–329 °C).

3. Galenobismutite and bismuthinite occur associated with fractures of the second generation of arsenopyrite. The lower experimental temperatures for these Bi minerals are within the temperature range for the second generation of arsenopyrite.

4. There are no significant distinctions in compositions of gold–silver alloy associated with fractures and filling spaces between grains of different arsenopyrite generations and included in quartz.

5. $\delta^{34}S$ mean values of arsenopyrite (− 4.7‰) and pyrite (− 3.8‰) are compatible with an ore-forming fluid of metamorphic and meteoric origin.

6. He–Ar isotopic data indicate that fluids have a dominant crustal origin and Ne and Ar isotopic ratios are atmospheric.

7. The ascent of the granite magma has provided the heat source for convective water circulation to remove gold–silver alloy, other metals and metalloids from the metamorphic rocks.

8. The abundance of aqueous carbonic fluids, the existence of aqueous low-salinity fluids and their minimum possible entrapment temperature (Th_{tot}) suggest that the gold-forming event initiated during the waning stages of the Variscan orogeny and happened at the transition from a lithostatic to an hydrostatic pressure gradient.

9. The depositions of gold–silver alloy took place during the decrease of temperature and pressure and in the remobilization stage.

10. This quartz arsenopyrite-gold deposit compares well with other quartz arsenopyrite-gold deposits from the Iberian Massif, but contains tungstates.

11. The Santo António mine is a gold deposit, younger than ca. 310 Ma, controlled by ductile to brittle-ductile deformation due to Variscan shearing and brittle deformation.

12. This deposit it has several characteristics that contradict a genetic assignment to the "intrusion-related" type, namely: (1) location in a large pluton (> 50 km^2 in area), (2) location in an elongated pluton, (3) no regional mineralogical zonation is observed with As–Au at the center of the pluton, followed by As–Sb–Au and Ag–Pb–Zn associations further, (4) the deposit has a gold content that cannot be considered low, (5) pyrrhotite is not the dominate sulphide, (6) very negative sulfur isotopes are not characteristic of a magmatic derivation, (7) there are no characteristically magmatic fluids with boiling indications, (8) initial fluids, typical of metamorphism are followed by meteoric fluids.

Acknowledgements This research was financially supported by *Fundação para a Ciência e Tecnologia* through the projects GOLD-Granites, Orogenesis, Long-term strain/stress and Deposition of ore metals—PTDC/GEO-GEO/2446/2012: COMPETE: FCOMP-01-0124-FEDER-029192 and UID/GEO/04035/2013. Thanks are due to *Colt Resources* for having allowed sampling in the Santo António gold mine and Dr. Pedro Keil for having helped in this field work, Profs. Martim Chichorro, José Brandão Silva and Rubén Díez-Fernández for constructive discussions in the field, Dr. J.M. Farinha Ramos for helpful information, Prof. R. Machado Leite for the use of electron microprobe at LNEG, Eng. Fernanda Guimarães for having helped to obtain analyses with this equipment, Dr. Manuel Moreira for the He–Ne–Ar isotopic data, Prof. R.A. Creaser for the Re content of pyrite and Dr. Armanda Dória for having helped with the Raman analysis. Thanks are also due to the editor and reviewers for their comments to help improve this manuscript.

Compliance with ethical standards

Conflict of interest There is no conflict of interest.

References

Alcock, J. E., Martínez Catalán, J. R., Rubio Pascual, F. J., Montes, A. D., Díez Fernández, R., Gómez Barreiro, J., et al. (2015). 2-D thermal modeling of HT-LP metamorphism in NW and Central Iberia: Implications for Variscan magmatism, rheology of the lithosphere and orogenic evolution. *Tectonophysics, 657,* 21–37.

Amcoff, O. (1976). The solubility of silver and antimony in galena. *Neues Jahrbuch für Mineralogie, 6,* 247–261.

Arias, D., Corretgé, L. G., Villa, L., Gallastegui, G., Suárez, O., & Cuesta, A. (1997). A sulphur isotopic study of the Navia gold belt (Spain). *Journal of Geochemical Exploration, 59,* 1–10.

Bakker, R. J. (1999). Adaptation of the Bowers and Helgeson (1983) equation of state to the H_2O–CO_2–CH_4–N_2–NaCl system. *Chemical Geology, 154,* 225–236.

Bakker, R. J. (2003). Package FLUIDS 1. Computer programs for analysis of fluid inclusion data and for modeling bulk fluid properties. *Chemical Geology, 194,* 3–23.

Bodnar, R. J. (1993). Revised equation and table for determining the freezing point depression of H_2O–NaCl solutions. *Geochimica et Cosmochimica Acta, 57,* 683–684.

Bodnar, R. J., Lecumberri-Sanchez, P., Moncada, D., & Steele-MacInnis, M. (2014). Fluid inclusions in hydrothermal ore deposits. In H. D. Holland & K. K. Turekian (Eds.), *Treatise on geochemistry* (2nd ed., Vol. 13, pp. 119–142). Oxford: Elsevier.

Boiron, M. C., Barakat, A., Cathekineau, M., Banks, D. A., Durivosa, J., & Moravek, P. (2001). Geometry and P-V-T-X conditions of microfissural ore fluid migration: The Mokrsko gold deposit (Bohemia). *Chemical Geology, 173,* 207–225.

Boiron, M. C., Cathelineau, M., Banks, D. A., Fourcade, S., & Vallance, J. (2003). Mixing of metamorphic and surficial fluids during the uplift of the Hercynian upper crust: Consequences of gold deposition. *Chemical Geology, 194,* 119–141.

Boiron, M.-C., Cathelineau, M., Banks, D. A., Yardley, B. W. D., Noronha, F., & Miller, M. F. (1996). P-T-X conditions of late Hercynian fluid penetration and the origin of granite-hosted gold quartz veins in northwestern Iberia: A multidisciplinary study of fluid inclusions and their chemistry. *Geochimica et Cosmochimica Acta, 60,* 43–57.

Boiron, M. C., Essaraj, S., Sellier, E., Cathelineau, M., Lespinasse, M., & Poty, B. (1992). Identification of fluid inclusions in relation to their host microstructural domains in quartz by cathodoluminescence. *Geochimica et Cosmochimica Acta, 56,* 175–185.

Bowers, T. S., & Helgeson, H. C. (1983). Calculation of the thermodynamic and geochemical consequences of nonideal mixing in the system H_2O–CO_2–NaCl on phase relations in geological systems: Equation of state for H_2O–CO_2–NaCl fluids at high pressures and temperatures. *Geochimica et Cosmochimica Acta, 47,* 1247–1275.

Burrows, D. R., & Spooner, E. T. C. (1989). Relationships between Archean gold vein-shear zone mineralisation and igneous intrusions in the Val d'Or and Timmins area, Abitibi Subprovince, Canada. *Economic Geology Monographs, 6,* 424–444.

Cathelineau, M., Boiron, M.C., Palomero, F.G., Urbano, R., Florido, P., Pereira, E.S., et al. (1993). *Multidisciplinary studies of Au-vein formation. Application to the western part of the Hesperian massif (Spain–Portugal)*. Final report, EEC project MA2M-CT90-0033.

Cave, B. J., Pitcairn, I. K., Craw, D., Large, R. R., Thompson, J. M., & Johnson, S. C. (2017). A metamorphic mineral source for tungsten in the turbidite-hosted orogenic gold deposits of the Otago Schist, New Zealand. *Mineralium Deposita, 52,* 515–537.

Chang, L. L. Y., & Hoda, S. H. (1977). Phase relations in the system PbS–Cu_2S–Bi_2S_3 and the stability of galenobismutite. *American Mineralogist, 62,* 346–350.

Cook, N. J., Ciobanu, C. L., Meria, D., Silcock, D., & Wade, B. (2013). Arasenopyrite-pyrite association in an orogenic gold ore: Tracing mineralization history from textures and trace elements. *Economic Geology, 108,* 1273–1283.

Corfu, F. (2004). U–Pb age, setting and tectonic significance of the anorthosite–mangerite–charnockite–granite suite, Lofoten–Vesterälen, Norway. *Journal of Petrology, 56,* 2081–2097.

Cotelo Neiva, J. M., & Neiva, A. M. R. (1990). The gold area of Jales (northern Portugal). *Terra Nova, 2,* 243–254.

Couto, H., Roger, G., & Borges, F. S. (2007). Late Paleozoic orogenic gold-antimony deposits from the Dúrico-Beirã area (North Portugal): Relation with hidden granite apexes. In C. J. Andrew et al (Eds.), *Proc. ninth Biennal meeting of the society for geology applied to mineral deposits, Ireland* (Vol. 1, pp. 609–615). Cambridge: Cambridge Mineral Resources.

Couto, H., Roger, G., Moëlo, Y., & Bril, H. (1990). Le district à antimoine-or Dúrico Beirão (Portugal): Évolution paragénétique et géochimique: Implications métallogéniques. *Mineralium Deposita, 25*(Suppl), 569–581.

Craig, J. R., Vokes, F. M., & Solberg, T. N. (1993). Pyrite: Physical and chemical textures. *Mineralium Deposita, 34,* 82–101.

D'Angelico, A. J., Jenkin, G. R. T., & James, D. (2016). Orogenic gold mineralization in northwest Iberia, Portugal: Role of metasediment source as a control on location, geochemistry and mineralogy. *Applied Earth Science, 125,* 73–74.

Dallmeyer, R. D., Martínez Catalán, J. R., Arenas, R., Gil Ibarguchi, J. J., Gutiérrez-Alonso, G., Farias, P., et al. (1997). Diachronous Variscan tectonothermal activity in the NW Iberian Massif: Evidence from $^{40}Ar/^{39}Ar$ dating of regional fabrics. *Tectonophysics, 277,* 307–337.

Davis, D. W., Blackburn, C. E., & Krogh, T. E. (1982). Zircon U–Pb ages from Wabigoon, Manitou Lakes region, Wabigoon subprovince, northwest Ontario. *Canadian Journal of Earth Sciences, 19,* 254–266.

Dee, S. J., & Roberts, S. (1993). Late-Kinematic gold mineralization during regional uplift and the role of nitrogen: An example from the La Codosera area, W. Spain. *Mineralogical Magazine, 57,* 437–450.

Dias, G., Leterrier, J., Mendes, A., Simões, P. P., & Bertrand, J. M. (1998). U-Pb zircon and monazite geochronology of post-collisional Hercynian granitoids from the Central Iberian Zone (Northern Portugal). *Lithos*, *45*, 349–369.

Díez Balda, M. A., Martínez Catalán, J. R., & Ayarza, P. (1995). Syn-collisional extensional collapse parallel to the orogenic trend in a domain of steep tectonics—The Salamanca detachment zone (Central Iberian Zone, Spain). *Journal of Structural Geology, 17,* 163–182.

Díez Fernández, R., & Arenas, R. (2015). The Late Devonian Variscan suture of the Iberian Massif: A correlation of high-pressure belts in NW and SW Iberia. *Tectonophysics, 654,* 96–100.

Díez Fernández, R., Gómez Barreiro, J., Martínez Catalán, J. R., & Ayarza, P. (2013). Crustal thickening and attenuation as revealed by regional fold interference patterns: Ciudad Rodrigo basement area (Salamanca, Spain). *Journal of Structural Geology, 46,* 115–128.

Díez Fernández, R., & Pereira, M. F. (2016). Extensional orogenic collapse captured by strike-slip tectonics: Constrains from structural geology and U–Pb geochronology of the Pinhel shear zone (Variscan orogen, Iberian Massif). *Tectonophysics, 691,* 290–310.

Díez Fernández, R., & Pereira, M. F. (2017). Strike-slip shear zones of the Iberian Massif: Are they coeval? *Lithosphere, 9,* 726–744. https://doi.org/10.1130/L648.1.

Escuder Viruete, J. E., Arenas, R., & Martínez Catalán, J. R. (1994). Tectonothermal evolution associated with Variscan crustal extension in the Tormes gneiss dome (NW Salamanca, Iberian massif, Spain). *Tectonophysics, 23,* 117–138.

Escuder Viruete, J., Hernáiz Huerta, P. P., Valverde-Vaquero, P., Rodríguez Fernández, R., & Dunning, G. (1998). Variscan syncollisional extension in the Iberian Massif: Structural, metamorphic and geochronological evidence from the Somosierra sector of the Sierra de Guadarrama (Central Iberian Zone, Spain). *Tectonophysics, 290,* 87–109.

Ferreira, N., & Sousa, M. B. (1994). Notícia explicativa da folha 14-B da Carta Geológica de Portugal (scale 1/50000; Moimenta da Beira). Serviços Geológicos de Portugal. Folha 14-B, 53 p

Fischer, N. H. (1945). The fineness of gold with special reference to the Morobe goldfield, New Guinea. *Economic Geology, 40,* 449–495.

Fuertes-Fuente, M., Cepedal, A., Lima, A., Dória, A., Ribeiro, M. J., & Guedes, A. (2016). The Au-bearing vein system of the Limarinho deposit (northern Portugal): Genetic constraints from Bi-chalcogenides and Bi–Pb–Ag sulfosalts, fluid inclusions and stable isotopes. *Ore Geology Reviews, 72,* 213–231.

Gamond, J. F., & Giraud, A. (1982). Identification des zones de faille á l'aide des associations de fractures de second ordre. *Bulletin de la Société Géologique de France, 24,* 755–762.

Garofalo, P. S., & Ridley, J. R. (2014). Gold-transporting hydrothermal fluids in the Earth's crust: An introduction. In P. S. Garofalo & J. R. Riddley (Eds.), *Gold-transportation hydrothermal fluids in the Earth's crust* (Vol. 402, pp. 1–7). London: The Geological Society Special Publications.

Gilfillan, S., Ballentine, C., Holland, G., Blagburn, D., Sherwood, B., Lollar, B., et al. (2008). The noble gas geochemistry of natural CO_2 gas reservoirs from the Colorado Plateau and Rocky Mountain provinces, USA. *Geochimica et Cosmochimica Acta, 72,* 1174–1198.

Goldfarb, R. J., Baker, T., Dube, B., Gorves, D. L., Hart, C. J. R., & Gosselin, P. (2005). Distribution, character, and genesis of gold deposits in metamorphic terranes. *Economic Geology, 100th Anniversary Volume,* 407–450.

Goldfarb, R. J., & Groves, D. I. (2015). Orogenic gold: Common or evolving fluid and neutral sources through time. *Lithos, 233,* 2–26.

Goldfarb, R. J., Groves, D. I., & Gardoll, S. (2001). Orogenic gold and geologic time: A global synthesis. *Ore Geology Reviews, 18,* 1–75.

Goldfarb, R. J., Newberry, R. J., Pickthorn, W. J., & Gent, C. A. (1991). Oxygen, hydrogen, and sulfur isotope studies in the Juneau gold belt, southeastern Alaska: Constraints on the origin of hydrothermal fluids. *Economic Geology, 86,* 66–80.

Gómez-Fernández, F., Vindel, E., Martín-Crespo, T., Sánchez, V., González Clavijo, E., & Matías, R. (2012). The Llamas de Cabrera gold district, a new discovery in the Variscan basement of northwest Spain: A fluid inclusion and stable isotope study. *Ore Geology Reviews, 46,* 68–82.

Graupner, T., Niedermann, S., Kempe, U., Klemd, R., & Bechtel, A. (2006). Origin of ore fluids in the Muruntau gold system: Constraints from noble gas, carbon isotope and halogen data. *Geochimica et Cosmochimica Acta, 70*(21), 5356–5370.

Graupner, T., Niedermann, S., Rhede, D., Kempe, U., Seltmann, R., Williams, C. T., et al. (2010). Multiple sources for mineralizing fluids in the Charmitan gold(-tungsten) mineralization (Uzbekistan). *Mineralium Deposita, 45,* 667–682.

Groves, D. I., Gordfarb, R. J., Knox-Robinson, C. M., Ojala, J., Gardoll, S., Yun, G. Y., et al. (2000). Late-kinematic timing of orogenic gold deposits and significance for computer-based exploration techniques with emphasis on the Yilgarn Block, Western Australia. *Ore Geology Reviews, 17,* 1–38.

Gunter, F. (1986). *Principles of isotope geology* (2nd ed.). New York: Wiley.

Jaffey, A. H., Flynn, K. F., Glendenin, L. E., Bentley, W. C., & Essling, A. M. (1971). Precision measurement of half-lives and specific activities of ^{235}U and ^{238}U. *Physical Review, Section C Nuclear Physics, 4,* 1889–1906.

Kendrick, M. A., Burgess, R., Pattrick, R. A. D., & Turner, G. (2001). Fluid inclusion noble gas and halogen evidence on the origin of Cu-porphyry mineralizing fluids. *Geochimica et Cosmochimica Acta, 65,* 2651–2668.

Kendrick, M. A., & Burnard, P. (2013). Noble gases and halogens in fluid inclusions: A journey through the Earth's crust. In P. Burnard (Ed.), *The noble gases as geochemical tracers, advances in isotope geochemistry*. Berlin: Springer.

Kendrick, M. A., Honda, M., Walshe, J., & Petersen, K. (2011). Fluid sources and the role of abiogenic-CH_4 in Archean gold mineralization: Constraints from noble gases and halogens. *Precambrian Research, 189,* 313–327.

Kim, K. H., Lee, S., Nagao, K., Sumino, H., Yang, K., & Lee, J. I. (2012). He–Ar–H–O isotopic signatures in Au–Ag bearing ore fluids of the Sunshin epithermal gold–silver ore deposits, South Korea. *Chemical Geology, 320–321,* 128–139.

Knight, C. L., & Bodnar, R. J. (1989). Synthetic fluid inclusions: IX. Critical PVTX properties of NaCl–H_2O solutions. *Geochimica et Cosmochimica Acta, 53,* 3–8.

Kretschmar, U., & Scott, S. D. (1976). Phase relations involving arsenopyrite in the system Fe–As–S and their application. *Canadian Mineralogist, 14,* 364–386.

Krogh, T. E. (1973). A low contamination method for hydrothermal decomposition of zircon and extraction of U and Pb for isotopic age determinations. *Geochimica et Cosmochimica Acta, 37,* 485–494.

Krogh, T. E. (1982). Improve accuracy of U–Pb zircon ages by creation of more concordant systems using an air abrasion technique. *Geochimica et Cosmochimica Acta, 46,* 637–649.

Lang, J. R., & Baker, T. (2001). Intrusion-related gold systems: The present level of understanding. *Mineralium Deposita, 36,* 477–489.

Lawrence, D. M., Treloar, P. J., Rankin, A., Boyce, A., & Harbidge, P. (2013a). A fluid inclusion and stable isotope study at the Loulo Mining District, Mali, West Africa: Implications for multifluid sources in the generation of orogenic gold deposits. *Economic Geology, 108,* 229–257.

Lawrence, D. M., Treloar, P. J., Rankin, A. H., Harbidge, P., & Holliday, J. (2013b). The geology and mineralogy of the Loulo Mining District, Mali, West Africa: Evidence for two distinct styles of orogenic gold mineralization. *Economic Geology, 108,* 199–227.

Leal Gomes, C. (1994). Estudo estrutural e paragenético de um sistema pegmatoide granítico. – O campo aplito-pegmatítico de Arga – Minho (Portugal). *Unpublished PhD thesis, Univ. Minho, Portugal*.

Leal Gomes, C. (1997). Estruturas de deformação Hercínica tardia na transição D3–D4 – evidência e interpretação de marcadores mineralógicos, marcadores litológicos, objectos geométricos simples e critérios cinemáticos – discussão da viabilidade de isolamento de um episódio deformacional D'3 (D3-tardio) na vertente oriental da Serra de Arga – Minho – N de Portugal. "Livro guia da excursão pós-reunião". In C. Coke (Ed.) *PICG 376—XIV Reunião de Geologia do Oeste Peninsular* (pp. 97–118).

Leal Gomes, C. (2000a). Análise comparativa das paragéneses auríferas nos índices, Dacotim, Fonte do Coxo, Bouções e Turgueira – área de Penedono – *relatório inédito para Rio Narcea Gold Mines – filial portuguesa, Penedono*.

Leal Gomes, C. (2000b). Análise paragenética e tipologia das expressões auríferas do depósito de Santo António-Vieiros (Penedono) – *relatório inédito para Rio Narcea Gold Mines – filial portuguesa, Penedono*.

Leal Gomes, C., & Castelo Branco, J. M. (2003). Tipologia do particulado aurífero tardio nas mineralizações de Penedono (Viseu, Portugal). In *IV Congresso Ibérico de Geoquímica e XIII Semana de Geoquímica, Livro de Resumos* (pp. 190–192).

Leal Gomes, C., & Gaspar, O. C. (1992). Mineralizações filonianas associadas a cisalhamentos pós-pegmatóides do campo aplito-pegmatítico de Arga – Minho. *Comunicações dos Serviços Geológicos de Portugal, 78,* 31–47.

Lee, J. Y., Marti, K., Severinghaus, J. P., Kawamura, K., Yoo, H. S., Lee, J. B., et al. (2006). A redetermination of the isotopic abundances of atmospheric Ar. *Geochimica et Cosmochimica Acta, 70,* 4507–4512.

Liu, C., Liu, J., Carranza, E. J. M., Yang, L., Wang, J., Zhai, D., et al. (2016). Geological and geochemical constraints on the genesis of the Huachanggou gold deposit, western Qinling region, central China. *Ore Geology Reviews, 73,* 354–373.

Llana-Fúnez, S., & Marcos, A. (2001). The Malpica–Lamego Line: A major crustal scale shear zone in the Variscan belt of Iberian. *Journal of Structural Geology, 23,* 1015–1030.

López-Moro, F. J., López-Plaza, M., Gutíerrez-Alonso, G., Fernández-Suárez, J., López-Carmona, A., Hofmann, M., et al. (2017). Crustal melting and recycling: Geochronology and sources of Variscan syn-kinematic anatectic granitoids of the Tormes Dome (Central Iberian Zone). A U–Pb LA–ICP–MS study. *International Journal of Earth Sciences*. https://doi.org/10.1007/s00531-017-1483-8.

Ludwig, K. R. (2003). *Users manual for Isoplot 3.00* (Vol. 4). Berkeley: Geochronology Center Special Publications.

Marcoux, E., Nerci, K., Branquet, Y., Ramboz, C., Ruffet, G., Peucat, J.-J., et al. (2015). Late-Hercynian intrusion-related gold deposits: An integrated model on the Tighza polymetallic district, central Morocco. *Journal of African Earth Sciences, 107,* 65–88.

Martínez Catalán, J. R., Arenas, R., Abati, J., Sánchez Martínez, S., Díaz García, F., Fernández-Suárez, J., et al. (2009). A rootless suture and the loss of the roots of a mountain chain: The 1159 Variscan belt of NW Iberia. *Comptes Rendus Geoscience, 341,* 114–126.

Martínez Catalán, J. R., Arenas, R., Díaz Garcia, F., & Abati, J. (1997). Variscan accretionary complex of northwest Iberia: Terrane correlation and succession of tectonothermal events. *Geology, 25,* 1103–1106.

Martínez Catalán, J. R., Rubio Pascual, F. J., Díez, Montes A., Díez, Fernández R., Gómez, Barreiro J., Dias da Silva, Í., et al. (2014). The late Variscan HT/LP metamorphic event in NW and Central Iberia: Relationships to crustal thickening, extension, orocline development and crustal evolution. *Geological Society, London, Special Publications, 405,* 225–247.

Mikucki, E. J. (1998). Hydrothermal transport and depositional processes in Archean lode-gold systems: A review. *Ore Geology Reviews, 13,* 307–321.

Morey, A. A., Tomkins, A. G., Bierlein, F. G., Weinberg, R. F., & Davidson, G. J. (2008). Bimodal distribution of gold in pyrite and arsenopyrite: Example from the Archean Boorara and Bardoc shear zones, Yilgarn craton, Western Australia. *Economic Geology, 103,* 599–614.

Murphy, P. J., & Roberts, S. (1997). Evolution of a metamorphic fluid and its role in lode gold mineralization in the Central Iberian Zone. *Mineralium Deposita, 32,* 459–474.

Neiva, A. M. R. (1994). Gold-quartz veins at Gralheira, northern Portugal: Mineralogical and geochemical characteristics. *Transactions of the Institution of Mining and Metallurgy. Section B. Applied Earth Science, 103,* B188–B196.

Neiva, A. M. R., András, P., & Ramos, J. M. F. (2008). Antimony quartz and antimony-gold quartz veins from northern Portugal. *Ore Geology Reviews, 34,* 533–546.

Nogueira, P., & Noronha, F. (1993). A evolução de fluidos hidrotermais associados a mineralizações de (Au–Ag–As) em contexto granítico. Os exemplos de Grovelas e Penedono, norte de Portugal. Mem. nº 3, Univ. Porto, Fac. Ciênc., Mus. Lab. Mineral. Geol. In F. Noronha, M. Marques & P. Nogueira (Eds.), *IX Semana de Geoquímica e II Cong. Geoquímica dos países de língua portuguesa* (pp. 275–278).

Noronha, F., Cathelineau, M., Boiron, M.-C., Banks, D. A., Dória, A., Ribeiro, M. A., et al. (2000). A three stage fluid flow model for Variscan gold metallogenesis in northern Portugal. *Journal of Geochemical Exploration, 71,* 209–224.

Ohmoto, H., & Goldhaber, M. B. (1997). Sulfur and carbon isotopes. In H. I. Barnes (Ed.), *Geochemistry of hydrothermal ore deposits* (3rd ed., pp. 517–612). New York: Wiley.

Oliveira, J. T. (1992). Carta Geológica de Portugal, Folha Norte, scale 1/500 000. Serv. Geol. Portugal, Moimenta da Beira, 53 p.

Ortega, L., & Vindel, E. (1995). Evolution of ore forming fluids associated with late Hercynian antimony deposits in central/western Spain: Case study of Maria Rosa and El Juncalón. *European Journal of Mineralogy, 7,* 655–673.

Ozima, M., & Podosek, F. A. (2002). *Noble gas geochemistry*. Cambridge: Cambridge University Press.

Pereira, I., Dias, R., Santos, T. B., & Mata, J. (2017). Exhumation of a migmatite complex along a transpessive shear zone: Inferences from the Variscan Juzbado–Penalva do Castelo Shear Zone (Central Iberian Zone). *Journal of the Geological Society*. https://doi.org/10.1144/pgs2016-159.

Pereira, M. F., Díez Fernández, R., Gama, C., Hofmann, M., Gärtner, A., & Linnemann, U. (2018). S-type granite generation and emplacement during a regional switch from extensional to contractional deformation (Central Iberian Zone, Iberian autochthonous domain, Variscan Orogeny). *International Journal of Earth Sciences, 107,* 251–267. https://doi.org/10.1007/s00531-017-1488-3.

Pettke, T., Frei, R., Kramers, J. D., & Villa, I. M. (1997). Isotope systematics in vein gold from Brusson, Val d'Ayas (NW Italy). 2. (U + Th)/He and K/Ar in native Au and its fluid inclusions. *Chemical Geology, 135,* 173–187.

Pitcairn, I. R., Teagle, D. A., Craw, G. R., Olivo, G. R., Kerrich, R., & Brewer, T. S. (2006). Sources of metals and fluids in orogenic gold deposits: Insights from the Otageo and Alpine Schists, New Zealand. *Economic Geology, 101,* 1525–1546.

Pokrovski, G. S., Akinfiev, N. N., Borisova, A. Y., Zotov, A. V., & Kouzmanov, K. (2014). Gold speciation and transport in geological fluids: Insights from experiments and physical–chemical modelling. In P. S. Garofalo & J. R. Ridley (Eds.), *Gold-transporting hydrothermal fluids in the Earth's crust* (Vol. 42, pp. 9–70). London: The Geological Society Special Publications.

Poty, B., Leroy, J., & Jachimowicz, L. (1976). Un novel appareil pour la mesure des températures sous le microscope: L'installation de microthermométrie Chaixmeca. *Bulletin de Minéralogie, 99,* 182–186.

Prieto, A. C., Guedes, A., Dória, A., Noronha, F., & Jiménez, J. (2012). Quantitative determination of gaseous phase compositions in fluid inclusions by Raman microspectrometry. *Spectroscopy Letters, 45,* 156–160.

Rauchenstein-Martinek, K., Wagner, T., Wälle, M., & Heinrich, C. A. (2014). Gold concentrations in metamorphic fluids: A LA-ICPMS study of fluid inclusions from the Alpine orogenic belt. *Chemical Geology, 385,* 70–83.

Regêncio Macedo, C. A. (1988). Granitoids, Complexo Xisto-Grauváquico e Ordovícico na região entre Trancoso e Pinhel (Portugal Central): Geologia, Petrologia, Geocronologia. *Unpublished PhD thesis, Univ. Coimbra, Coimbra, Portugal*, p. 430.

Roedder, E. (1984). Fluid inclusions. In Paul H. Ribbe (Ed.), *Reviews in mineralogy* (Vol. 12). Chantilly: Mineralogical Society of America.

Romberger, S. B. (1986). The solution chemistry of gold applied to the origin of hydrothermal deposits. In L. A. Clark (Ed.), *Gold in the western Shield, special volume* (pp. 168–186). Montreal: Canadian Institute of Mining and Metallurgy.

Sharp, Z. D., Essene, E. J., & Kelly, W. C. (1985). A re-examination of the arsenopyrite geothermometer: Pressure considerations and applications to natural assemblages. *Canadian Mineralogist, 23,* 517–534.

Shepherd, T. (1981). Temperature-programmable heating-freezing stage for microthermometric analysis of fluid inclusions. *Economic Geology, 76,* 1244–1247.

Shepherd, T., Rankin, A., & Alderton, D. (1985). *A practical guide to fluid inclusions studies*. London: Blackie and Son Lda.

Sibson, R. (1973). Interactions between temperature and pore-fluid pressure during earthquake faulting and a mechanism for partial or total stress relief. *Nature, 243,* 66–68.

Sibson, R. (1983). Continental fault structure and the shallow earthquake source. *Journal of the Geological Society of London, 140,* 741–767.

Sibson, R. (1987). Earthquake rupturing as a mineralizing agent in hydrothermal systems. *Geology, 15,* 701–704.

Sibson, R. (1990). Faulting and fluid flow. In B. E. Nesbitt (Ed.), *Fluids in tectonically active regimes of the continental crust. Short course handbook, 18. Mineral. As.* Vancouver (pp. 93–132).

Sibson, R., McM, Moore, & Rankin, A. (1975). Seismic pumping—A hydrothermal fluid transport mechanism. *Journal of the Geological Society of London, 131,* 653–659.

Silva, A. F., & Ribeiro, M. L. (1991). Carta Geológica de Portugal, scale 1:50 000, Notícia explicativa da Folha 15-A Vila Nova de Foz Côa. Instituto Geológico e Mineiro, 52 p.

Silva, A. F., & Ribeiro, M. L. (1994). Carta Geológica de Portugal, scale 1:50 000, Notícia explicativa da Folha 15-B Freixo de Espada à Cinta. Instituto Geológico e Mineiro, 48 p.

Simmons, S. F., Sawkins, F. J., & Schlutter, D. J. (1987). Mantle derived helium in two Peruvian hydrothermal ore deposits. *Nature, 329,* 429–432.

Sousa, M. B., & Ramos, J. M. F. (1991). Características geológico-estruturais e químico-mineralógicas das jazidas auríferas da região de Penedono-Tabuaço (Viseu, Portugal). *Estudos Notas e Trabalhos, D.G.G.M., 33,* 71–96.

Sousa, M. B., & Sequeira, A. J. D. (1989). Notícia explicativa da folha 10-D da Carta Geológica de Portugal (scale 1/50 000; Alijó). Serv. Geol. Portugal, 59 p.

Stacey, J. S., & Kramers, J. D. (1975). Approximation of terrestrial lead isotope evolution by a low-stage model. *Earth and Planetary Science Letters, 34,* 207–226.

Stefánsson, A., & Seward, T. M. (2003). Experimental determination of the stability and stoichiometry of sulphide complexes of silver (I) in hydrothermal solutions to 400 °C. *Geochimica et Cosmochimica Acta, 67,* 1395–1413.

Stefánsson, A., & Seward, T. M. (2004). Gold(I) complexing in aqueous sulphide solutions to 500 °C at 500 bar. *Geochimica et Cosmochimica Acta, 68,* 4121–4143.

Stuart, F. M., Burnard, P., Taylor, R. P., & Turner, G. (1995). Resolving mantle and crustal contributions to ancient hydrothermal fluid: He–Ar isotopes in fluid inclusions from Dae Hwa W-Mo mineralization, South Korea. *Geochimica et Cosmochimica Acta, 59,* 4663–4673.

Sundlab, K., Zachrisson, E., Smeds, S. A., Berglund, S., & Alinder, C. (1984). Sphalerite geobarometry and arsenopyrite geothermometry applied to metamorphosed sulfide ores in the Swedish Caledonides. *Economic Geology, 79,* 1660–1668.

Tornos, F., Spiro, B. F., Shepherd, T. Y., & Ribera, F. (1997). Sandstone-hosted lodes of the southern West Asturian Leonese Zone (NW Spain). *Chronique de la Recherche Minière, 528,* 71–86.

Ueda, A. H. R. K. (1986). Direct conversion of sulphide and sulphate minerals to SO_2 for isotope analysis. *Geochemical Journal, 20,* 209–212.

Valkiers, S., Vendelbo, D., Berglund, M., & Podesta, M. (2010). Preparation of argon primary measurement standards for the calibration of ion current ratios measured in argon. *International Journal of Mass Spectrometry, 291,* 41–47.

Vallance, J., Cathelineau, M., Boiron, M. C., Fourcade, S., Shepherd, T. J., & Naden, J. (2003). Fluid–rock interactions and the role of late Hercynian aplite intrusion in the genesis of the Castromil gold deposit, northern Portugal. *Chemical Geology, 194,* 201–224.

Valle Aguado, B., Azevedo, M. R., Schaltegger, U., Martínez Catalán, J. R., & Nolan, J. (2005). U–Pb zircon and monazite geochronology of Variscan magmatism related to syn-convergence extension in Central Northern Portugal. *Lithos, 82,* 169–184.

Zhai, W., Sun, X., Wu, Y., Sun, Y., Hua, R., & Ye, X. (2012). He–Ar isotope geochemistry of the Yaoling-Meiziwo tungsten deposit, North Guangdong Province: Constraints on Yanshanian crust-mantle interaction and metallogenesis in SE China. *Chinese Science Bulletin, 57*(10), 1150–1159.

Affiliations

Ana M. R. Neiva[1,2] · António Moura[3] · Carlos A. Leal Gomes[4] · Manuel Francisco Pereira[5] · Fernando Corfu[6]

✉ António Moura
ajmoura@fc.up.pt

[1] Geobiotec, Departamento de Geociências, Universidade de Aveiro, 3810-193 Aveiro, Portugal

[2] Departamento de Ciências da Terra, Universidade de Coimbra, 3030-780 Coimbra, Portugal

[3] Instituto de Ciências da Terra (ICT), Departamento de Geociências, Ambiente e Ordenamento do Território, Faculdade de Ciências, Universidade do Porto, Rua do Campo Alegre, 687, 4099-007 Porto, Portugal

[4] Departamento de Ciências da Terra, Universidade do Minho, Gualtar, 4710-057 Braga, Portugal

[5] Instituto de Ciências da Terra (ICT), Departamento de Geociências, ECT, Universidade de Évora, 7000-671 Évora, Portugal

[6] Department of Geosciences and CEED, University of Oslo, PB1047, Blindern, 0316 Oslo, Norway